ORIGINAL PAPER

Elastic thermobarometry on metapelites across the crustal section of the Famatinian Arc, Argentina

Emanuel Giovanini[1,4] · Kenneth S. Befus[1,5] · Juan E. Otamendi[2] · Eber Cristofolini[2] · Tomas Guerreiro[2] · Miguel Cisneros[3]

Abstract

We applied elastic thermobarometry on garnet-bearing migmatites along two transects through the crustal section at Sierra Valle Fértil-La Huerta, Argentina. We performed quartz-in-garnet barometry and zircon-in-garnet thermometry on metapelites from different paleo-depths across the crustal section. Our work recovers entrapment pressures ranging from 240 to 1330 MPa and entrapment temperatures between 691 and 1574 °C. The entrapment conditions are broadly consistent with anticipated pressures and temperatures along the crustal section derived previously using conventional, thermodynamic thermobarometers. The quartz-in-garnet barometer reproduces those conventionally established entrapment conditions when samples only experienced conditions within the alpha-quartz stability field. Raman-derived pressures for samples that experienced beta-quartz reference conditions are commonly much higher than those established by conventional barometry. Samples that preserve compressive (positive) residual pressures best reproduce reference entrapment pressures. Entrapment temperatures show high variability and overestimation of temperature conditions compared to conventional results. These results indicate elastic thermobarometry over- or under-estimates crystallization conditions in rocks crystallized at high temperatures, as is common in the Famatinian Arc deep-crust. We suggest that modeling quartz behavior across the alpha–beta transition may present challenges, as does shape maturation, viscous deformation, and radiation damage in zircon.

Keywords Elastic thermobarometry · Famatinian Arc · Migmatites · Quartz-in-garnet barometry · Zircon-in-garnet thermometry

✉ Emanuel Giovanini
egiovanini@ethz.ch

1 Department of Geosciences, Baylor University, Waco, TX, USA

2 CONICET, Departamento de Geología, Universidad Nacional de Río Cuarto, Río Cuarto, Argentina

3 Lawrence Livermore National Laboratory, Livermore, CA, USA

4 Present Address: Department of Earth Sciences, Institute for Geochemistry and Petrology, ETH Zürich, Zürich, Switzerland

5 Present Address: Earth and Planetary Sciences, Jackson School of Geosciences, University of Texas at Austin, Austin, TX, USA

Introduction

Mountain building, tectonics, volcanic activity, and their associated hazards are produced by the imbalance of geologic forces. Direct physical measurements of the responsible processes are impossible because they take place deep in the Earth's subsurface. Our understanding of processes in these subsurface environments has relied on indirect methods like geophysical surveys, geochemical analyses, and geodynamics (Rawlinson et al. 2010; Li and Liebermann 2014). Petrology and mineralogy provide additional records of subsurface processes that rely upon crystals as passive record keepers within these dynamic systems. Crystals provide valuable in-situ information because their textures and compositions respond to environmental changes like deformation, pressure, and temperature (e.g., Kretz 1959; Ferry and Spear 1978; Spear et al. 1984; Essene 1989; Platt and Behr 2011; Lanari and Engi 2017).

The estimation of pressure–temperature (P–T) conditions of rocks is fundamental for understanding petrologic and tectonic processes. Many thermometers and barometers have been developed to constrain the P–T conditions of mineral nucleation (e.g., Kretz 1959; Spear et al. 1990). Most thermobarometers rely on the presumption of achieving local partition, net-transfer, chemical or isotopic equilibrium between a certain number of mineral phases to calculated P–T conditions (e.g., Selverstone and Spear 1985; Powell and Holland 1994, 2008; Pattison and Tinkham 2009). We refer to these methods as 'conventional thermobarometry' (e.g., Powell 1985; Powell and Holland 1994, 2008; Moecher and Sharp 1999). Some examples of conventional approaches are stable isotope thermometry (e.g., Javoy 1977; Moecher and Sharp 1999; Valley 2001), cation-exchange thermobarometry (e.g., Ferry and Spear 1978; Tomkins et al. 2007; Thomas et al. 2010), or trace elements thermometry (e.g., Zack et al. 2004; Ferry and Watson 2007; Spear et al. 2012). However, recent advances have revealed that the nucleation and growth of certain mineral phases, such as garnet, may require overstepping of metamorphic reactions (e.g., Spear et al. 2014; Castro and Spear 2017; Spear and Wolfe 2019, 2020). As a result, equilibrium-based calculations reflect disequilibrium conditions during prograde metamorphism, underestimating the true peak conditions (e.g., Carlson 2002; Lanari and Engi 2017; Wolfe and Spear 2018).

Technological advances in the field of spectroscopy have facilitated the development and application of 'elastic thermobarometry' (e.g., Enami et al. 2007; Kohn 2014; Spear et al. 2014; Castro and Spear 2017; Angel et al. 2017b; Spear and Wolfe 2020; Wolfe and Spear 2020; Kohn et al. 2023). Elastic thermobarometry only relies on the physical/elastic properties of minerals and attainment of mechanical equilibrium, and is independent of chemical and isotopic equilibrium requirements (Fig. 1). This technique takes advantage of the difference in the physical properties between a solid mineral inclusion and its host to calculate the pressure and temperature conditions during their nucleation (e.g., Adams et al. 1975; Angel et al. 2015b, 2017b; Cisneros and Befus 2020). Elastic thermobarometry was developed decades ago (Rosenfeld and Chase 1961), but its use has rapidly increased in the past decade because Raman spectroscopy now provides a relatively straightforward, low-cost approach to measuring residual pressures preserved by solid mineral inclusions (e.g., Nasdala et al. 2004; Enami et al. 2007; Enami 2012; Korsakov et al. 2020; Cizina et al. 2023; Gonzalez et al. 2024). By combining the residual inclusion pressure with elastic models of an inclusion-host system, the conditions of entrapment can be calculated (e.g., Rosenfeld and Chase 1961; Angel et al. 2015b; Mazzucchelli et al. 2021; Kohn et al. 2023). Some inclusion-host pairs have emerged as community favorites because of their demonstrated ability to accurately constrain P–T conditions (e.g., Ashley et al. 2014; Zhong et al. 2019). Foremost is quartz-in-garnet, commonly abbreviated as QuiG in the literature, because it has been shown to be an excellent barometer through natural samples and synthetic experiments (e.g., Kohn 2014; Ashley et al. 2016; Castro and Spear 2017; Thomas and Spear 2018; Spear and Wolfe 2020; Wolfe and Spear 2020). Zircon-in-garnet (ZiG) has demonstrated efficacy as a thermometer (Zhong et al. 2019; Campomenosi et al. 2021). However, both techniques exhibit limitations, highlighting the need for complementary information from other conventional methods to fully comprehend the entire evolution of the rock. These limitations include metamictisation processes on zircon inclusions (Campomenosi
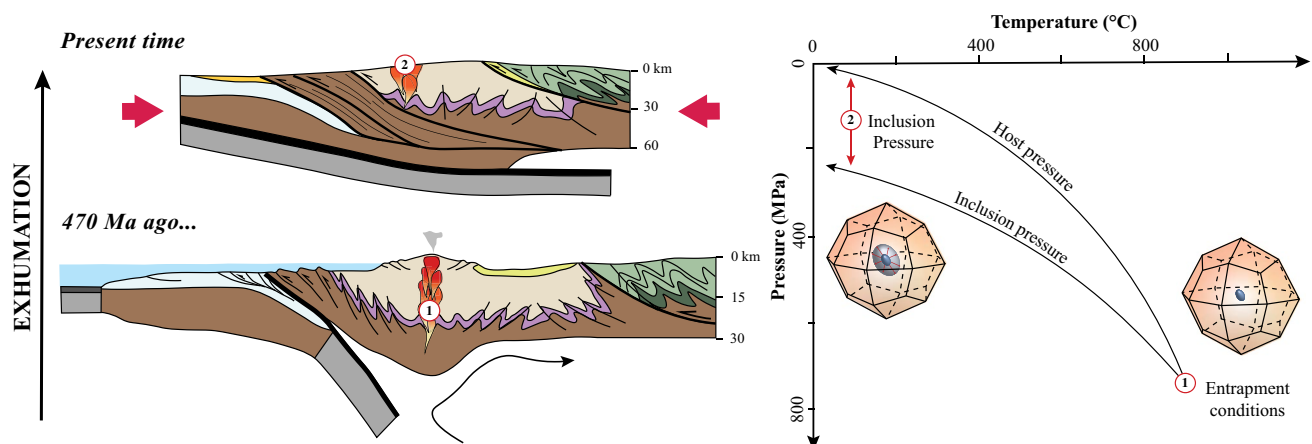

Fig. 1 Schematic P–T path of a crystalline inclusion-host system during cooling and exhumation from crystallization at location 1 to location 2 at the Earth's surface. The mineral inclusion is subjected to overpressure because it remains confined inside the host mineral, creating a residual inclusion pressure

et al. 2020), post-entrapment modifications like viscous relaxation and plastic yield (Zhong et al. 2020; Campomenosi et al. 2021, 2023), or non-ideal inclusions geometries (Mazzucchelli et al. 2018, 2019; Zhong et al. 2019, 2020).

Recent contributions to elastic thermobarometry have focused on the development of precise mineral elasticity models, advanced analytical instrumentation, and exploring mineral host-inclusion pairs (e.g., Angel et al. 2015a, 2017b, 2019; Campomenosi et al. 2018; Mazzucchelli et al. 2019, 2021; Cisneros and Befus 2020; Gonzalez et al. 2021, 2024; Kohn et al. 2023). Studies have also focused on testing if elastic thermobarometry can constrain P–T conditions of crystallization in geological settings where conventional, equilibrium-based thermobarometers were not suitable (e.g., Castro and Spear 2017; Wolfe and Spear 2018, 2020; Barkoff et al. 2019; Spear and Wolfe 2019, 2020; Guo et al. 2021; Cisneros et al. 2022). To date, elastic thermobarometry has been shown to be reliable based on laboratory synthesis experiments of garnets around quartz, and reproducibility of known synthesis conditions (e. g., Thomas and Spear 2018; Bonazzi et al. 2019; Gonzalez et al. 2024). Studies that use natural samples have typically applied the technique over a restricted range of P–T conditions and host types: including, in diamond- or garnet-hosted inclusions (e.g., Angel et al. 2015a; Gonzalez et al. 2019; Nestola et al. 2019; Alvaro et al. 2020), ultrahigh/high pressure metamorphic rocks from subduction zones (e.g., Ashley et al. 2014; Castro and Spear 2017; Baldwin et al. 2021; Harvey et al. 2021; Cisneros et al. 2021; Wolfe et al. 2023), and orogenic terranes (e.g., Wolfe and Spear 2018, 2020; Wolfe et al. 2021; Kośmińska et al. 2022). Elastic thermobarometry (e.g., quartz-in-garnet barometry), remains largely untested across P/T domains where quartz exist within the beta stability field, and no studies have systematically analyzed the suitability of the technique across large-scale geologic systems, such as magmatic arcs that cover a wide range of P–T conditions. In this work we thus performed elastic thermobarometry on metapelitic rocks along two transects that span the full crustal section of the Famatinian Arc, preserved in the rugged mountains of Valle Fértil-La Huerta, Argentina (Tibaldi et al. 2013; Camilletti et al. 2020; Otamendi et al. 2020). We targeted garnet-bearing migmatites for quartz-in-garnet barometry (QuiG) and zircon-in-garnet thermometry (ZiG), and compare our elastic thermobarometry results with reference P–T conditions established using conventional thermobarometry (Otamendi et al. 2008; Tibaldi et al. 2013; Mulcahy et al. 2014; Camilletti et al. 2020). Zircon-in-garnet thermometry is unreliable in our samples because all zircons are overly softened by metamictisation. Quartz-in-garnet elastic thermobarometry is broadly consistent with anticipated temperatures and pressures across the crustal section, but we show that the technique becomes limited-to-inaccurate at high temperatures.

Geologic background

The Famatinian orogen in northwestern Argentina represents the fossil record of an Early Paleozoic subduction zone that bounded on the Iapetus oceanic margin of western Gondwana (Ducea et al. 2017; Rapela et al. 2018; Otamendi et al. 2020; Cornet et al. 2022; Fig. 2a). This magmatic belt and orogenic system preserves the entire evolution of a magmatic arc, called the Famatinian Arc. This segment is represented by an extensive plutonic-volcanic belt that longitudinally extends 2000 km across western Argentina from southern Bolivia to northern Patagonia (20°–33° S) (Rapela et al. 2018; Otamendi et al. 2020). The Famatinian Arc was an east-dipping subduction zone (29°–32° S) on the proto-Andean margin from the Late Cambrian to Middle Ordovician (495–466 Ma), with a magmatic peak at ~470 Ma (Ducea et al. 2017; Rapela et al. 2018; Escribano et al. 2022). The bulk of the arc crust was constructed and emplaced by magmatism over a period of 20 Ma. This magmatic activity ended around 466 Ma when the Cuyania-Precordillera continental microplate collided against the western margin of Gondwana (Thomas and Astini 1996; Astini and Dávila 2004; Otamendi et al. 2009b; Ramos 2018).

As exposed over the Central Andean foreland, the modern stratigraphic and lithologic record of the Famatinian Arc is complex and variable along its extent as it was affected by several major tectonic cycles after the Ordovician (Otamendi et al. 2009b, 2020). Along-strike exposures of the Famatinian Arc display a gradient of paleo-depths, which allow direct geologic observations of the arc's evolution from its pre-Ordovician crust configuration to its episode of arc magmatism, continental convergence, and its final orogenic collapse (Otamendi et al. 2020). In the north (20–28 °S), outcrops present a geographically dispersed, but locally thick, succession of shallow crustal and volcano-sedimentary successions that formed during the early stages of the magmatic arc (Ducea et al. 2017; Armas et al. 2018, 2021; Otamendi et al. 2020; Cornet et al. 2022). Deeper rocks, including the crystalline basement produced and modified by the Famatinian Arc, are exposed in the south (28–33 °S). Basement exposures occur as regional-scale batholiths intercalated with high-grade metamorphic rocks (Otamendi et al. 2008; Tibaldi et al. 2013).

One of the most important outcrops of lower-middle crust basement exposure of the Famatinian Arc is located in a 120 × 30 km mountainous region called the Sierra Valle Fértil-La Huerta (Fig. 2b). Conventional thermobarometric estimates for crystallization conditions, geophysical studies, and petrological constraints have shown that the Sierra Valle Fértil-La Huerta is a continuous
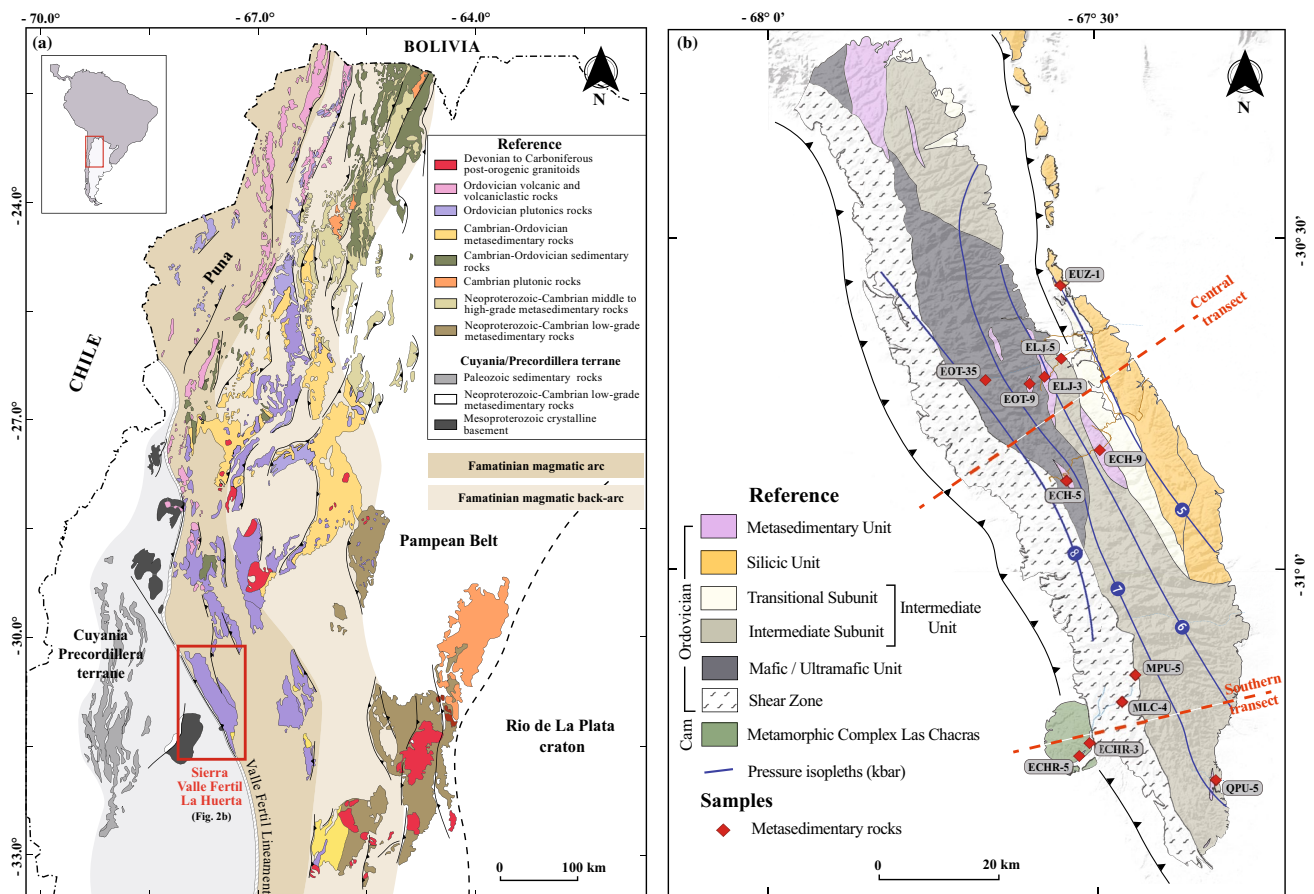
Fig. 2 **a** Simplified geologic map of northwestern Argentina showing the distribution of lithologic units associated with the Famatinian Arc evolution (modified from Otamendi et al. 2020). **b** Simplified geologic map of the study area with the location of metapelitic samples used for quartz-in-garnet and zircon-in-garnet thermobarometry. Red

dashed lines indicate the central and southern transects made during the sample collection. Pressure isopleths for paleodepth of the Sierra Valle Fértil–La Huerta are shown based on previous studies (Otamendi et al. 2008; Tibaldi et al. 2013; Camilletti et al. 2020)

exposure of the arc's crustal section at paleodepths of 15 to 40 km (Otamendi et al. 2008; Tibaldi et al. 2011, 2013). Collisional tilting and deformation along the Valle Fértil shear zone in the west from the lower Ordovician to Devonian (~465–400 Ma) have resulted in modern exposure of the crustal section, which now preserves a cross-sectional view of primary igneous and metamorphic structures that decrease in the magnitude of exhumation from west to east (van Staal et al. 2011; Otamendi et al. 2012; Cristofolini et al. 2014). The Loma de Las Chacras block outcrops immediately to the west of the Valle Fértil shear zone, on the west side of the Sierra Valle Fértil-La Huerta range (Fig. 2b). The Loma de Las Chacras block is an exceptionally preserved part of the fore-arc outboard along the Famatinian Arc (Casquet et al. 2012). Overall, this igneous and metasedimentary complex was initially subducted to great depths (>45 km) during tectonic contraction around 465 Ma (Mulcahy et al. 2014). The block then detached in the subduction channel and was ultimately

uplifted by tectonic extrusion from Silurian until lower Devonian (~435–407 Ma) (Mulcahy et al. 2014; Cristofolini et al. 2014).

The crustal section of the Famatinian Arc exposed in the Sierra Valle Fértil-La Huerta section is dominated by magmatic rocks interspersed by subordinate metasedimentary rocks (Otamendi et al. 2008, 2009b, 2012). There is no true stratigraphy preserved, however detailed mapping and geochemical analyses have shown the system grades from mafic to silicic units with decreasing paleo-depth (Otamendi et al. 2009b, 2012; Tibaldi et al. 2013; Walker et al. 2015; Camilletti et al. 2020, 2023). Past studies have revealed four major lithological units. A ~10-km-wide mafic unit dominantly composed of amphibole gabbronorites, and quartz-poor diorites occurs on the west and central area of Sierra Valle Fértil-La Huerta. Chilled mafic sills, dykes and enclaves intrude through the unit, and rare ultramafic-to-mafic bodies (peridotite, olivine gabbronorite, anortosite) are also dispersed within the gabbronorites. Thermobarometry places

the "mafic" rocks at 700–800 MPa and 850–900 °C, indicating that these rocks represent the deepest portion of the arc (Otamendi et al. 2010, 2016; Tibaldi et al. 2013; Fig. 3). Up section, an intermediate unit composed of heterogeneous bodies of amphibole- and biotite-bearing tonalites and diorites stretches along the central region of the Sierra Valle Fértil-La Huerta. Its thickness varies, but generally narrows from ~20 km in the south to ~10 km in the north (Otamendi et al. 2009a; Camilletti et al. 2020, 2023). The intermediate unit is sometimes intruded by syn-plutonic leucogranitic dikes and preserves magmatic enclaves and metasedimentary xenoliths (Camilletti et al. 2020). A silicic unit composed of batholith-scale granodiorites, monzogranites, and leucogranites occurs adjacent to the eastern boundary of Sierra Valle Fértil –La Huerta and overlays the intermediate unit. The silicic unit is characterized by N-S-trending aligned plutons, which exhibit either inequigranular texture or porphyritic K-feldspar texture. Silicic plutonic rocks contain variable amounts of dioritic and gabbroic enclaves and dykes, as well as migmatite xenoliths (Ducea et al. 2017; Camilletti et al. 2020, 2023). Finally, a discontinuous metasedimentary unit composed of garnet-sillimanite- and cordierite-bearing migmatites, with subordinate amounts of marble, occurs as decameter-to-kilometer-long lenses throughout the lower portions of the crustal section. These metasedimentary rocks are derived from greywacke, pelitic, and calcsilicate protoliths that were metamorphosed under granulite-facies metamorphism at 450–750 MPa and 600–900 °C (Otamendi et al. 2008; Tibaldi et al. 2011, 2013; Fig. 3).

Sample location and descriptions

Although the vast volumetric majority of the Sierra Valle Fértil-La Huerta consists of intrusive igneous rocks we sampled metapelitic and metagraywacke migmatites because they provide the most established targets for elastic thermobarometry. We collected 12 samples across two cross-sections: one transect crosses the center of the Sierra Valle Fértil ("Central Transect"), and the second transect in the south crosses through Sierra La Huerta and Sierra Loma de las Chacras ("Southern Transect") (Figs. 2b and 3).

The migmatites typically preserve discrete mesosomes and leucosomes of variable thickness (Table 1; Fig. 4a and b). Leucosomes show a granoblastic texture, with the leucogranitic composition dominated by quartz, plagioclase, K-feldspar and variable amounts of cordierite and garnet. The mesosomes most commonly present a
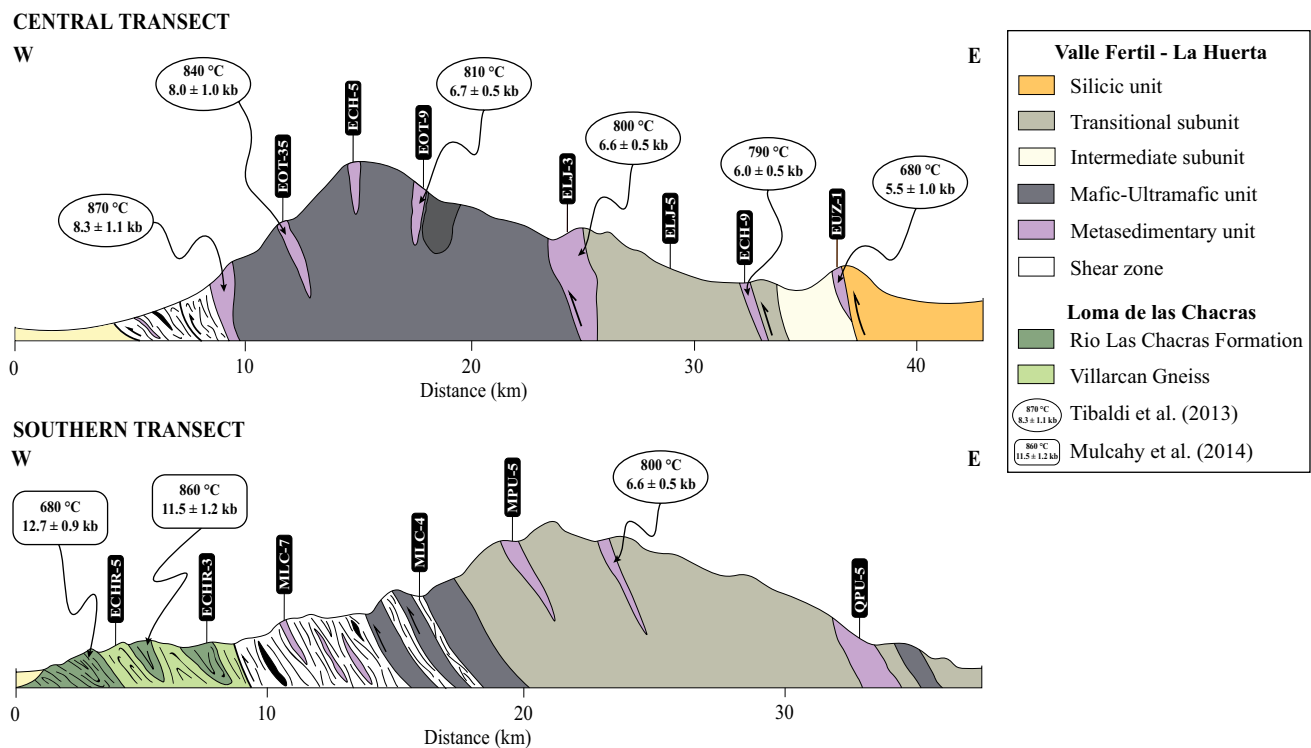

Fig. 3 5x-vertically exaggerated cross section across the central and southern part of Sierra Valle Fértil-La Huerta, showing the P–T conditions based on conventional thermobarometry (Otamendi et al. 2008; Tibaldi et al. 2011, 2013; Mulcahy et al. 2014) and locations of the samples used in this study. The Central Transect exposes shallow and middle crustal rocks but lacks the deepest portion of the section. The Southern Transect lacks the middle paleo-arc crustal section but contains the deep crust. Taken together the crustal sections provide a 30-km-thick window in a paleo-arc crust

Table 1 Sample locations, rock type, mineralogy, and reference P–T conditions for the samples used in this study

Sample	Location	Latitude	Longitude	Rock type	Mineralogy[a]	Reference P conditions (MPa)[b]	Reference T conditions (°C)[b]
EOT-35	Q. Otarola	−30.7077	−67.6611	Grt-bearing migmatite	Qz + Pl + Grt + Sill + Kfs (Ap-Zrn-Mag-Ser)	800 ± 55	840 ± 40
EOT-9	Q. Otarola	−30.7180	−67.6091	Grt-bearing migmatite	Qz + Pl + Grt + Bt + Ms + Kfs ± Sill (Ap-Zrn-Rt-Ser)	670 ± 50	810 ± 20
ELJ-3	Q. Las Juntas	−30.7156	−67.5843	Grt-bearing migmatite	Qz + Pl + Grt + Bt + Ms + Kfs ± Sill (Ap-Zrn-Rt-Mag)	660 ± 50	800 ± 20
ELJ-5	Q. Las Juntas	−30.6840	−67.5584	Grt-bearing migmatite	Qz + Pl + Grt + Bt + Ms + Kfs ± Sill (Ap-Zrn-Rt-Mag)	655 ± 45	790 ± 40
ECH-5	Q. Chavez	−30.8643	−67.5490	Crd-Grt-bearing migmatite	Qz + Pl + Crd + Grt + Bt + Kfs ± Sill (Ap-Zrn-Ser)	750 ± 50	820 ± 30
ECH-9	Q. Chavez	−30.8165	−67.5014	Crd-Grt-bearing migmatite	Qz + Pl + Crd + Grt + Bt + Kfs ± Sill (Zrn-Rt-Ser)	600 ± 50	790 ± 20
EUZ-1	Uzno	−30.5773	−67.5697	Crd-bearing migmatite	Qz + Pl + Crd + Bt + Kfs ± Grt (Zrn-Rt-Mag-Ser)	550 ± 100	700 ± 50
QPU-5	Q. Puesto	−31.3193	−67.3229	Grt-bearing migmatite	Qz + Pl + Grt + Bt + Kfs (Zrn-Ap-Mag-Ser)	700 ± 40	800 ± 20
MPU-5	Q. Puesto	−31.1604	−67.4466	Grt-bearing migmatite	Qz + Pl + Grt + Bt + Kfs (Zrn-Ap-Mag-Ser-Chl)	695 ± 35	815 ± 25
MLC-4	Q. Las Chacras	−31.2009	−67.4650	Grt-bearing migmatite	Qz + Pl + Grt + Bt + Kfs (Zrn-Ap-Rt-Ser)	785 ± 55	820 ± 30
ECHR-3	Loma de las Chacras	−31.2658	−67.5142	Grt-bearing migmatite	Qz + Pl + Grt + Ms + Bt + Kfs (Zrn-Ap-Rt-Ser)	1150 ± 50	805 ± 55
ECHR-5	Loma de las Chacras	−31.2845	−67.5285	Grt amphibolite	Amph + Pl + Qz + Grt (Ttn-Rt-Zrn)	1240 ± 60	680 ± 40

[a]Mineral abbreviations following Whitney and Evans (2010)

[b]Reference pressures (MPa) and temperatures (°C) from conventional thermobarometry based on Otamendi et al. (2008), Tibaldi et al. (2011, 2013), Mulcahy et al. (2014) and Camilletti et al. (2020)

granolepidoblastic texture that consists of quartz, plagioclase and biotite with variable amounts of sillimanite, cordierite, garnet, and Fe-Ti oxides. Migmatite bodies were classified into three main subtypes based on their mineral assemblages: (1) cordierite-bearing migmatites, (2) cordierite-garnet-sillimanite-bearing migmatites and (3) garnet-sillimanite-bearing migmatites (Otamendi et al. 2008; Tibaldi et al. 2013). The classification reflects the stratigraphic position as garnet-sillimanite-bearing migmatites prevail at deep crustal levels whereas cordierite-bearing migmatites prevail in the shallow crust.

Along the western border of the Sierra Valle Fértil-La Huerta, the crustal section is affected by significant deformation occurring as ductile-fragile strained and sheared fabrics produced by several mylonitic belts. Outcrops of the migmatites inside these belts present variable strain with pervasive mylonitic fabrics. Mylonites contain garnet and quartz-feldspar porphyroclasts set within a fine-grained matrix of biotite, quartz, plagioclase, muscovite and sillimanite. For this study, only samples with a low degree of deformation have been selected.

The Sierra Loma de Las Chacras, located on the west side of the Valle Fértil shear zone, preserves high-pressure metapelitic rocks. These rocks are not genetically related to the Sierra Valle Fértil-La Huerta metasedimentary unit and are instead tectonically juxtaposed on the southwestern margin of Sierra La Huerta through the Valle Fértil shear zone (Mulcahy et al. 2014; Cristofolini et al. 2014). Metapelites from Sierra Loma de Las Chacras consist of deformed metamorphic rocks in amphibolite to granulite facies. Migmatites constitute most of the outcrops and are interspersed with layers of ortho-amphibolite and schist. Migmatites have a well-defined foliation caused by the segregation of leucosomes and mesosomes. The leucosomes consist of quartz, K-feldspar, plagioclase, and garnet. The mesosomes contain garnet, kyanite, plagioclase, biotite, and quartz.

Garnets from Sierra Valle Fértil-La Huerta and Sierra Loma de Las Chacras occur as euhedral to subhedral porphyroblasts, ranging from 0.5 to 20 mm across (Fig. 4c and d). Solid inclusions in garnets from Sierra Valle Fértil-La Huerta are scarce, only occurring in sparse volumetric quantities of the garnet (<25%). When present, inclusions are quartz, zircon, biotite, amphibole, sillimanite, monazite, and rutile. In Sierra Loma de Las Chacras, the garnets are poikiloblastic with high concentrations of quartz, zircon, and amphibole inclusions. Inclusions do not present preferred orientation in any samples. Among the suite of observed inclusions hosted in the garnet, only quartz and zircon were suitable for elastic thermobarometry. Quartz inclusions are 10–500 μm across and can be
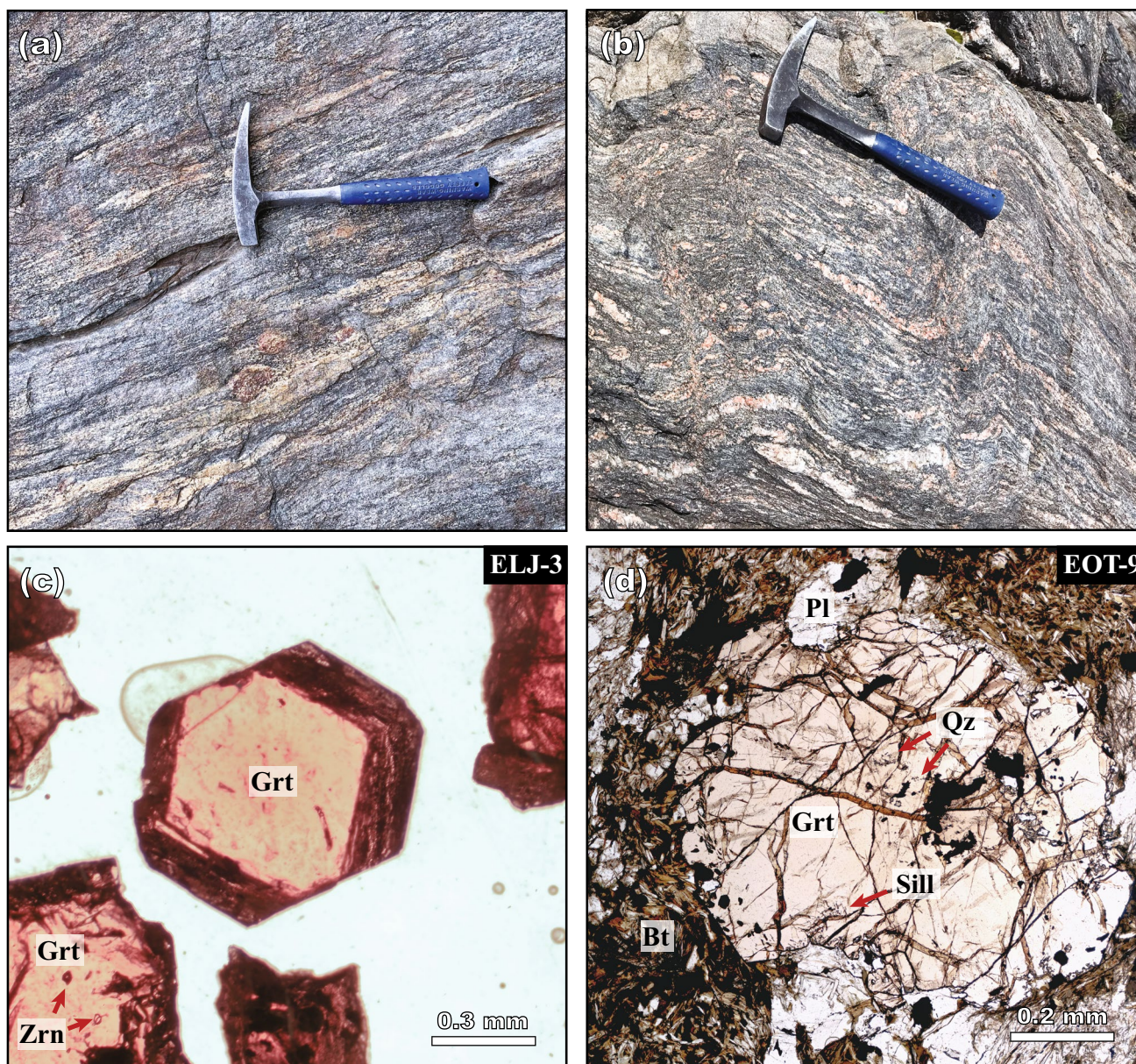
Fig. 4 a-b Field photographs of **a** typical garnet-bearing migmatites (Sample EOT-9) and **b** cordierite-garnet-bearing migmatites (Sample ECH-5) from Sierra Valle Fértil-La Huerta. These metapelitic rocks are predominantly metatexites with discreet mesosomes and leu- cosomes of variable thickness. **c** Photomicrograph of a garnet grain mount showing euhedral and anhedral crystals. **d** Photomicrograph of garnet-bearing migmatite showing a subhedral garnet porphyroblast

found in garnet cores and rims. The morphologies of the quartz inclusions vary greatly, occurring as polyhedrons, round ovoids, or irregular shapes. Zircon inclusions occur as elongate ovoid grains ranging from 10 to 60 μm in length. Sometimes they occur in clusters but they are always randomly oriented.

Analytical methods

We prepared 200-μm-thick sections and grain mounts using ~60 handpicked garnets from each sample, and then identified ~10 quartz and zircon inclusions hosted in those garnets. We performed Raman analyses of quartz and

zircon inclusions on two different instruments: a confocal Thermoscientific DXR at Baylor University and WiTec Alpha 300R instrument at Rutgers University. Analyses at Baylor University were done with a 532 nm laser, a high-resolution grating with 1800 lines mm^{-1}, a 200 μm confocal aperture, and a 25 μm pinhole slit width. We used a laser power of 4 mW and 50× objective to focus the beam on the inclusion with a spatial resolution of 0.7 μm. The spectral resolution is 1.2 cm^{-1} and the instrumental precision in the peak position determination is about 1 cm^{-1}. Analyses at Rutgers University were conducted with a 532 nm laser, a high-resolution grating with 1800 lines mm^{-1}, a 100× objective, and a 200 μm confocal aperture. This instrument has a spatial resolution of 0.1 μm and a spectral resolution of 0.6 cm^{-1} with a variable laser power that was set at 5 mW.

To avoid non-elastic stress modifications, we only targeted quartz and zircon inclusions that were isolated from one another and more than three times their radial distance from other inclusions, grain boundaries, and other defects (e.g., Angel et al. 2015b; Campomenosi et al. 2018; Mazzucchelli et al. 2019; Gonzalez et al. 2021). The beam was targeted near the center of inclusions to minimize the spectral effects produced by geometry and crystallographic orientation or anisotropy (Mazzucchelli et al. 2018). Zircons were analyzed in both core and rim positions to detect possible heterogeneity caused by oscillatory zoning (e.g., Campomenosi et al. 2020).

All Raman spectral data were fit using PeakFit 4.12 to identify band maxima and minimize analytical uncertainty (SYSTAT Software Inc). First a linear background subtraction was applied. Pseudo-Voigt functions were used to fit the quartz 128, 206, and 464 cm^{-1} bands, whereas Voigt models were used to fit the curvature of zircon bands at 201, 213, 224, 356, 438, 975, and 1008 cm^{-1} (Yuan and Mayanovic 2017; Cizina et al. 2023). For clarity, we use 'band' and 'peak' synonymously throughout. We then measured the peak position, full widths at half maximum (FWHM), and intensities on each Raman band (Fig. 5). The statistical uncertainty of the fitting functions varies with the width and intensity of the Raman peaks, and the instrumental uncertainty. Therefore, the resulting uncertainty of the 128 and 464 cm^{-1} bands for quartz are lower than 0.1 cm^{-1}, and the 206 cm^{-1} peak has an uncertainty of ~0.2 cm^{-1}. For zircon the resulting uncertainty is lower than 0.2 cm^{-1} for all peaks.

The Raman frequency shift ($\Delta\omega = \omega_{inc} - \omega_{ref}$) for quartz bands was determined relative to unstrained Herkimer quartz. Herkimer quartz is a hydrothermal quartz that occurs in limestones cavities in Herkimer County, NY, and is commonly used as reference standard for quartz studies
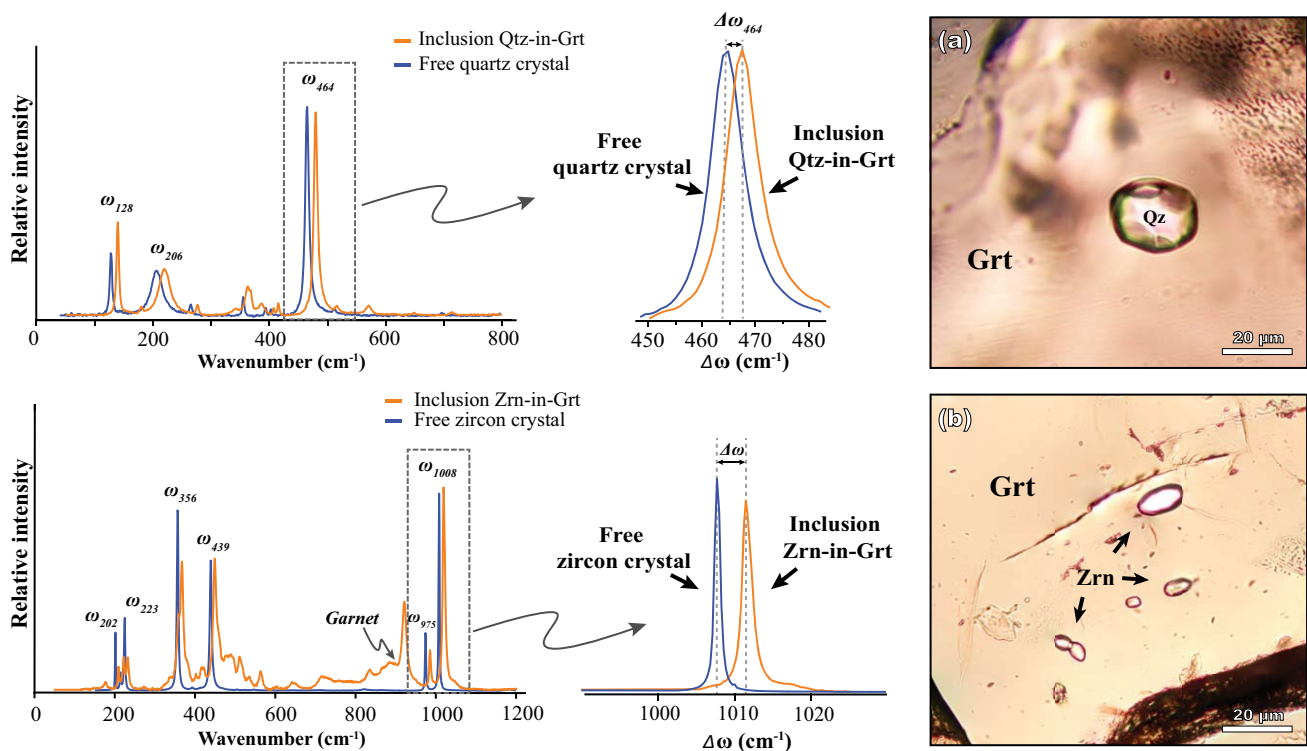

Fig. 5 Raman spectra of target quartz and zircon inclusions (*orange*), showing Raman frequency shift relative to Raman spectra of unstrained standard crystals (*blue*). **a** Photomicrograph of quartz inclusion in garnet with polyhedron shape (Sample ELJ-3). **b** Photomicrograph of zircon inclusions in garnet with ovoidal shapes (Sample QPU-5) (color figure online)

because of its undeformed crystal structure and homogeneous composition (Dunn and Fisher 1954; O'Reilly and Parnell 1999). Zircon bands were measured relative to NMNH 117288-3 zircon standard acquired from the Smithsonian Institution. These quartz and zircon crystal standards were measured several times throughout each analytical session to constrain instrumental drift (Cizina et al. 2023). Instrumental drift was observed and subsequently corrected using a time-dependent linear drift correction applied to the reference peak position for both Herkimer quartz and NMNH 117288-3 zircon (Supplementary File—Table S1 and Table S3).

We used Raman frequency shifts in quartz and zircon to calculate inclusion pressure (P_{inc}) following two established methods. In the first method, $\underline{P}_{inc}$ was calculated using pressure-dependent Raman shift calibrated by hydrostatic diamond anvil cell experiments (e.g., Ashley et al. 2014; Castro and Spear 2017; Wolfe and Spear 2018, 2020; Zhong et al. 2019; Spear and Wolfe 2019, 2020; Cisneros et al. 2021). For quartz inclusions, we used the pressure-dependent calibration of the 464, 208, and 128 cm^{-1} bands from Schmidt and Ziemann (2000). For zircon inclusions, we used the hydrostatic pressure-dependent calibration of the 1008, 975, and 456 cm^{-1} bands established by Zhong et al. (2019). We also calculated P_{inc} using a second numerical, theoretical approach that relies upon the minerals' Grüneisen tensors and Raman shifts using the *Strainman* software following Angel et al. (2019). After the strain was calculated, the mean stress and inclusion pressure ($P_{inc} = -(2\sigma_1 + \sigma_3)/3$) were then calculated using the *EntraPT* software, which converts strains into mean stress by applying an elasticity tensor at ambient P–T for quartz and zircon (Mazzucchelli et al. 2021). All P_{inc} were calculated by accounting for residual strain components at ambient temperature (Angel et al. 2019). We report P_{inc} from both approaches to best constrain entrapment conditions (strains methods have "S" superscript and hydrostatic calibrations approach have an "H" superscript).

To constrain the variability of elastic properties caused by the specific solid solution in the host mineral we analyzed garnet compositions using the Cameca SX Five electron microprobe at Texas A&M University. In each sample collected across the Sierra Valle Fértil-La Huerta approximately 5–10 garnets were analyzed. All microprobe analyses were conducted using 20 nA beam current with 15 keV accelerating voltage and a 3 μm spot diameter. Elements were counted for 20 s on peak and 10 s on background. Na was measured first in the sequence. A ZAF correction was applied during each analysis.

To calculate entrapment pressure and temperatures we used the *Solid Inclusion Calculator* MATLAB script by Cisneros and Befus (2020). This script uses a one-dimensional elastic model derived by Angel et al. (2017a) to calculate molar volume changes and entrapment conditions, based on the following equation:

$$\left[\left(\frac{V}{V_{trap}}\right)_{inc} - \left(\frac{V}{V_{trap}}\right)_{host}\right]\left(\frac{V_{trap}}{V_{foot}}\right)_{inc} = \frac{3}{4G_{host}}(P_{inc} - P_{ext})$$

(1)

where $(V/V_{trap})_{inc}$ and $(V/\underline{V}_{trap})_{host}$ are the molar volume ratios of the entrapped inclusion and the host at ambient conditions (V) and at initial conditions (V_{trap}). $(V_{trap}/V_{foot})_{inc}$ is the ratio of the inclusion molar volume at entrapment conditions and at ambient temperature along the inclusion-host equilibrium path (Angel et al. 2017b; Cisneros and Befus 2020). G_{host}, P_{ext}, and P_{inc} are the shear modulus of the host, the ambient pressure, and the inclusion pressure at ambient conditions, respectively. The entrapment conditions are determined by iteratively adjusting the molar volume of both phases at entrapment conditions (V_{trap}) until both sides of the equation are equal.

Molar volumes of almandine, spessartine, and pyrope were calculated using thermodynamic properties from Holland and Powell (2011) and Milani et al. (2017). Grossular molar volumes were calculated using the thermodynamic properties from Milani et al. (2017). Shear moduli for garnet end-members were derived from the following references: almandine and pyrope (Wang and Ji 2001), spessartine (Bass 1995), and grossular (Isaak et al. 1992). We accommodated garnet solid solution using a linear mixing of molar volumes and shear moduli of the garnet end-members. Quartz molar volumes were calculated using Angel et al. (2017a) thermodynamic properties and curved-boundary approach. Zircon molar volumes were calculated using thermodynamic properties from Bass (1995) and Ehlers et al. (2022). We emphasize that the presence of radioactive trace elements like Hf, U, Th, and Y can damage the structure of zircon and change its elastic properties (e.g., Zhang et al. 2000; Campomenosi et al. 2020).

Elastic thermobarometry relies upon the volume change between the host and inclusion based on a given temperature or pressure. Thus, an independent pressure or temperature estimate is needed to calculate the unknown entrapment variable. The P–T conditions of nucleation for the Sierra Valle Fértil-La Huerta and Sierra Loma de las Chacras have been carefully established in past studies which used an array of conventional thermodynamic thermobarometry techniques (Otamendi et al. 2008; Tibaldi et al. 2013; Mulcahy et al. 2014; Camilletti et al. 2023). We targeted our fieldwork so our samples were collected from the same outcrops where conventional thermodynamic thermobarometry was previously applied. In context of the geotherm and lithostatic gradient of the paleoarc, our spatial reproduction of sampling thus ensures the comparisons we use are far less than the ~50 °C and ~25 MPa uncertainty of temperatures

and pressures established by conventional thermobarometry. Our goal was not direct comparison at the hand sample scale, however, we acknowledge that such a comparative study would provide interesting insight into the effectiveness of both techniques.

Results

The garnets in metasedimentary rocks from Sierra Valle Fértil-La Huerta show a similar composition across the entire crust section, averaging $Alm_{62\pm4}Py_{27\pm7}Spes_{7\pm6}Gros_{4\pm2}$ (Supplementary File—Table S5 and Fig. S1). Garnets from ELJ-3 and ELJ-5 migmatites are uniquely enriched in MnO, and their composition is roughly $Alm_{40}Py_{15}Spes_{41}Gros_4$. For Sierra Loma de Las Chacras garnets we used compositions measured by Mulcahy et al. (2014) (ECHR-5—Amphibolite garnet is $Alm_{54}Py_{10}Spes_4Gros_{32}$ and ECHR-3—Villarcan Gneiss garnet is $Alm_{69}Py_{21}Spes_6Gros_4$). All garnets are compositionally uniform from the core to the rim, with only slight compositional variations observed in the outermost rim of rare crystals. Because inclusions were generally located close to garnet cores the slight compositional changes in the outermost layer were disregarded in this study.

Quartz-in-garnet barometry

Despite the relatively low abundance of quartz inclusions in the garnets, a total of 132 quartz inclusions from Sierra Valle Fértil-La Huerta and 18 quartz inclusions from Sierra Loma de las Chacras were analyzed via Raman spectroscopy (Supplementary File—Table S2). In rocks from Sierra Valle Fértil-La Huerta the Raman shift variability is considerable. Peak positions of the 128 ($\Delta\omega_{128}$), 206 ($\Delta\omega_{206}$), and 464 cm^{-1} ($\Delta\omega_{464}$) bands shift towards lower or higher wavenumbers relative to an unstrained Herkimer quartz reference. In most Sierra Valle Fértil-La Huerta samples the magnitude of the Raman shift also varies significantly even among inclusions hosted within crystals from the same hand sample. Quartz inclusions typically display negative shifts ranging from 0 to −4.8 cm^{-1} for $\Delta\omega_{464}$, 0 to −16.9 cm^{-1} for $\Delta\omega_{206}$, and 0 to −4.9 cm^{-1} for $\Delta\omega_{128}$ (Figs. 7 and 8). The ELJ-3 and ELJ-5 samples are the exception as their bands produce more consistent frequency shifts, ranging from −1.4 to 1.4 cm^{-1} for $\Delta\omega_{464}$, −2.9 to 5 cm^{-1} for $\Delta\omega_{206}$, and −1.6 to 0.9 cm^{-1} for $\Delta\omega_{128}$. Band shifts and variability are most consistent in samples from the Sierra Loma de las Chacras. They range from −0.6 to 1.9 cm^{-1} for $\Delta\omega_{464}$ band, −0.6 to 7.6 cm^{-1} for $\Delta\omega_{206}$ band, and −1.2 to 1.3 cm^{-1} for $\Delta\omega_{128}$ band. Importantly, samples from Sierra Loma de las Chacras predominantly display positive values.

Inclusion pressures (P_{inc}) calculated using hydrostatic calibrations for the 128, 206, and 464 cm^{-1} bands across southern and central crustal sections yield values of −526 to 187 MPa, −360 to 263 MPa, and −516 to 205 MPa, respectively. In most cases there are significant discrepancies between P_{inc} values calculated using the $\Delta\omega_{128}$, $\Delta\omega_{206}$ and $\Delta\omega_{464}$ shifts (Supplementary File—Fig. S2). Such discrepancies cause a single inclusion to produce variable entrapment pressures calculated using either approach (Figs. 6 and 7). It is also important to highlight that shift direction plays a crucial role, with negative shifts producing negative P_{inc} values and positive shifts yielding positive P_{inc} values.

Strain components also provide valuable information on the stress field around the inclusions. Quartz, characterized by its rhombohedral structure, exhibits two symmetry-independent strains: $\varepsilon_1 = \varepsilon_2$ representing the strain along the a and b axes of the unit cell, and ε_3 along the c-axis (Bonazzi et al. 2019). Raman frequency shifts relate to those strains, thus enabling their conversion into inclusion pressure. A positive volume strain indicates the presence of a tensile stress field, whereas a negative volume strain suggests the influence of a compressive stress field. Most quartz inclusions in garnets from Sierra Valle Fértil-La Huerta exist under a tensile stress field. Those in the Loma de las Chacras exist under a compressive stress field (Fig. 8). Quartz inclusions with large negative shifts exhibit positive volume strains that exceed 0.005. In addition, these inclusions present positive $\varepsilon_1 + \varepsilon_2$ strain components with large uncertainties. The ε_3 component also presents considerable uncertainties, and the magnitude varies across negative and positive values. In contrast, quartz inclusions with a positive frequency shift generally exhibit negative strain volumes, with some positive values lower than 0.002. The $\varepsilon_1 + \varepsilon_2$ and ε_3 strain components of these inclusions tend to be negative and present low uncertainty.

Variability and uncertainty in the strain components can produce significant uncertainties encountered in the subsequent calculation of entrapment pressures. The elastic model used for entrapment pressure (P_{trap}) calculations is strictly applied to spherical inclusions that are under isotropic strain (Angel et al. 2017a, b). Therefore, it is crucial to constrain the anisotropy of inclusions to evaluate the reliability of the entrapment calculation. We used the concept of elastic strain anisotropy defined by Gonzalez et al. (2019) to constrain the stress field around each inclusion:

$$A = \frac{\varepsilon_1 + \varepsilon_2}{2} - \varepsilon_3 \qquad (2)$$

where A is a measure of the elastic strain anisotropy. An inclusion under isotropic strains would have an elastic strain anisotropy near zero because the a and c axes of the quartz crystalline structure are equal in magnitude ($A \sim 0$). The larger the absolute value of the elastic strain anisotropy
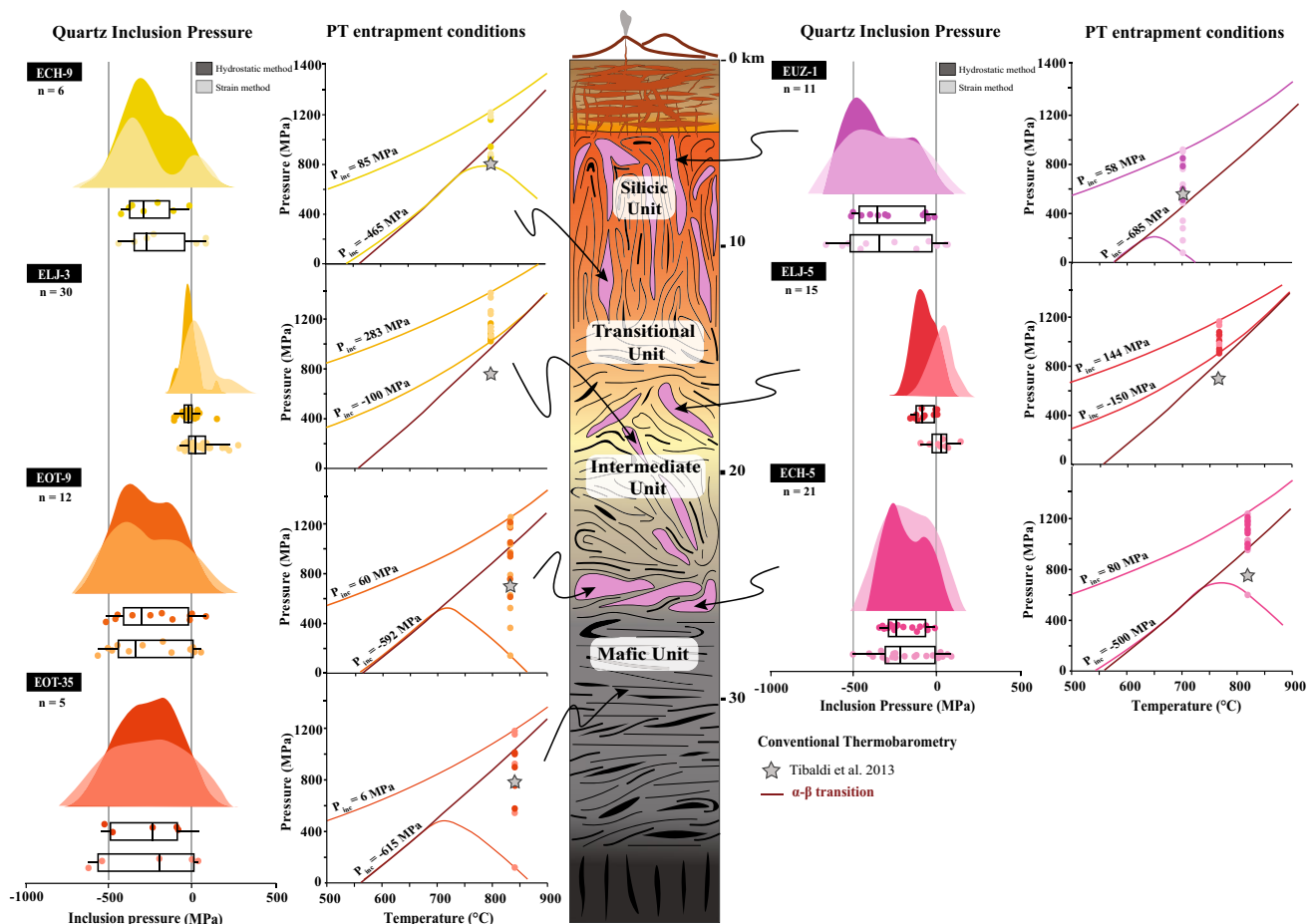
Fig. 6 Raincloud diagram of inclusion pressure distribution and calculated inclusion pressure isomekes of samples located on the central section. Relative location of each sample is indicated in a schematic reconstruction of the Famatinian Arc crustal section, showing the distribution of the different lithological units. Raincloud diagrams compare P_{inc} results from hydrostatic and strain components methods. Maximum and minimum P_{inc} are indicated with colored isomeke lines. The *colored points* indicate entrapment pressures constrained with previous temperature estimates from conventional thermobarometry (*gray stars*) (color figure online)

value, the bigger the strain difference between the axes. Elastic strain anisotropy values smaller than ±0.001 are commonly assumed to best represent isotropic strain. Despite purposefully selecting inclusions with spherical shape and spatial isolation, only 15 of the 150 quartz inclusions meet the criteria of being under an isotropic strain field. By arbitrary expanding the elastic isotropy-anisotropy threshold to ±0.003 we included an additional 30 inclusions (Fig. 8). These 45 inclusions should be best for thermobarometry. The remaining 70% of the inclusions present elastic strain anisotropy values ranging from −0.0198 to 0.020 and extend far outside the threshold for isotropic strain. Those inclusions should overestimate or underestimate P_{inc} thus creating discrepancies in thermobarometric results. Specifically, inclusions with negative elastic strain anisotropy will produce isomekes that overestimate P_{trap}, whereas inclusions

with positive elastic strain anisotropy produce isomekes that underestimate P_{trap} (Gonzalez et al. 2019).

Quartz inclusions produce a wide range of entrapment pressures ranging from 240 to 1330 MPa ($P_{trap}{}^{S}$) and 480 to 1270 MPa ($P_{trap-464}{}^{H}$). Although those estimates largely overlap the hydrostatic and strain tensor approaches do produce significant differences. The most pronounced disparities arise from inclusions with large negative shifts and can result in entrapment pressures that differ by more than 600 MPa. Elastic strain anisotropy plays an important role constraining the accuracy of the entrapment calculations. Entrapment pressures are most reliably reproduced by inclusions with the least anisotropy. The range of entrapment pressures reduces to 540 to 1120 MPa ($P_{trap}{}^{S}$) and 560 to 1115 MPa ($P_{trap-464}{}^{H}$) when only the most isotropic 15 inclusions are selected. When examined individually the hydrostatic and the strain tensor approaches best match in
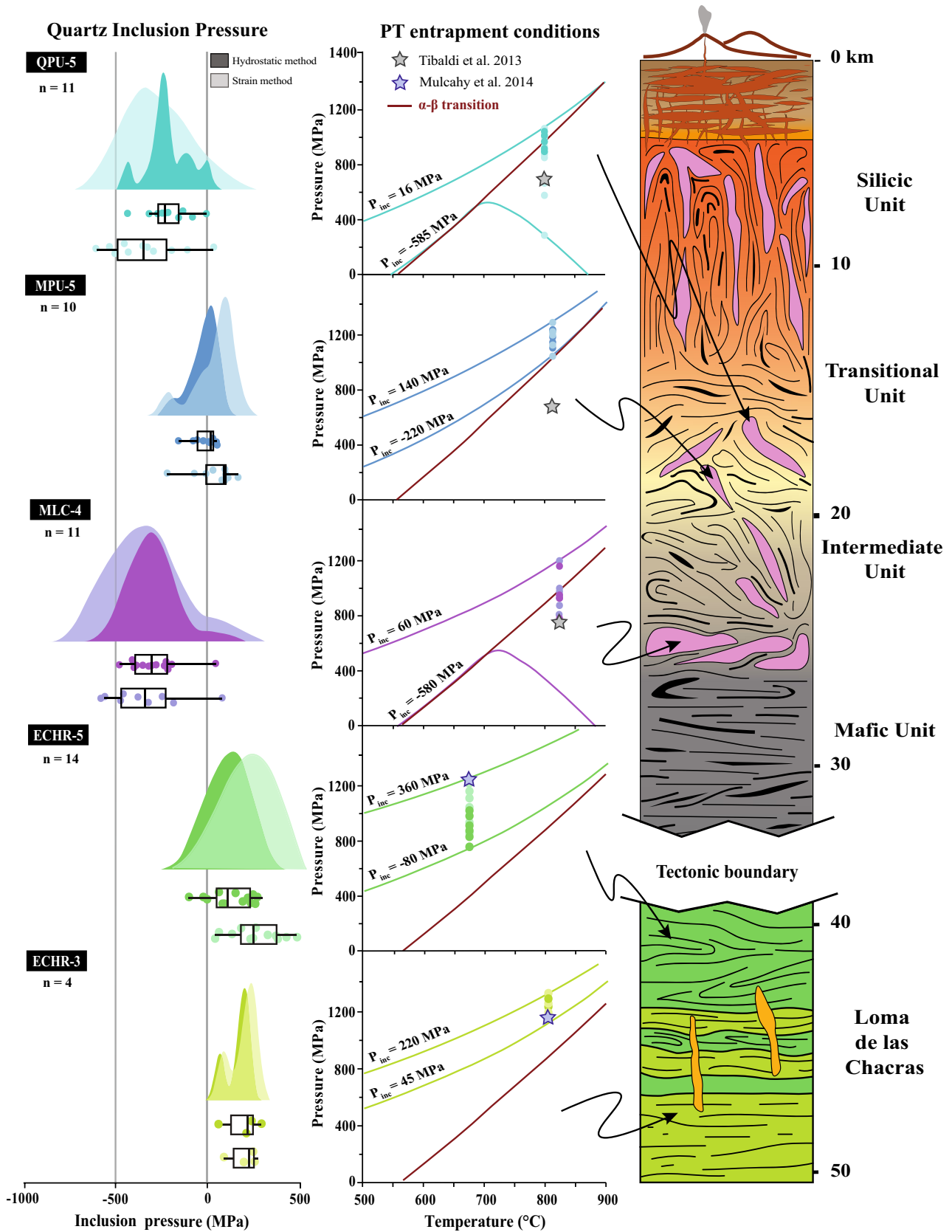
◂**Fig. 7** Continuing presentation from Fig. 6, now presenting the Southern transect. Relative location of each sample is indicated in a schematic reconstruction of the Famatinian Arc crustal section showing the distribution of the different lithological units. Raincloud diagrams compare P_{inc} results from hydrostatic and strain components methods. Maximum and minimum P_{inc} are indicated with colored isomekes lines. The *colored points* indicate entrapment pressures constrained with previous temperature estimates from conventional thermobarometry (*gray and blue stars*) (color figure online)

isotropic to near-isotropic inclusions, producing differences of <100 MPa (see whisker plots in Fig. 9). An example of the effect of inclusion isotropy can be demonstrated using EUZ-1 (Supplementary File—Table S2), which is known to have reached peak metamorphic conditions between 650 to 750 °C and 500 to 550 MPa (e.g., conventional thermobarometry from Tibaldi et al. 2013). An excellent match is produced using an inclusion with an isotropic strain ($A \sim 0$), with $P_{\text{trap-464}}^{H}$ of 561 MPa and P_{trap}^{S} of 544 MPa (R3). On the other hand, an inclusion with a highly negative elastic anisotropy of −0.0086 produces a $P_{\text{trap-464}}^{H}$ of 779 MPa and $P_{\text{trap-464}}^{S}$ of 899 MPa, overestimating entrapment pressure (B2). Another inclusion has a highly positive elastic anisotropy of 0.016, which calculated $P_{\text{trap-464}}^{H}$ of 494 MPa and P_{trap}^{S} of 196 MPa, both underestimating entrapment pressure (R2).

Failed Zircon-in-garnet thermometry

Zircon inclusions are abundant in garnets from Sierra Valle Fértil-La Huerta but rare in samples from Sierra Loma de las Chacras. A total of 63 zircon inclusions in garnets from the central transect of Sierra Valle Fértil-La Huerta were analyzed via Raman spectroscopy (Supplementary File—Table S4). Before estimating the inclusion pressure for each inclusion, we followed the protocol described by Campomenosi et al. (2020) to estimate the degree of radiation damage in the zircon crystals. The metamictisation, or self-radiation damage, in zircon can induce structural changes. Relative to pristine, undamaged crystals, radiation-damaged crystals exhibit Raman peaks that shift toward lower wavenumbers and broader peak widths (Binvignat et al. 2018; Campomenosi et al. 2020). To constrain the radiation damage in zircon, we measured the peak center and peak width in terms of full-width at half maximum (FWHM) for the 1008 cm^{-1} band. Inclusions produce FWHM predominantly between 4.1 and 10.6 cm^{-1}, with an average FWHM of 7.7 cm^{-1}. Moreover, the amount of radiation damage in a zircon crystal can be estimated by calculating the accumulation radiation doses, also known as α-dose. This parameter defined by Nasdala et al. (2001), is directly proportional to the concentration of U and Th and the age of the rocks. Almost all the zircon from Sierra Valle Fértil-La Huerta presents a FWHM of the 1008 cm^{-1} peak >4 cm^{-1}. Using data from previous chronologic studies in zircons from Sierra Valle Fértil-La Huerta (e.g., Ducea et al. 2017; Rapela et al. 2018; Cornet et al. 2022), we estimated accumulation radiation doses ranging from 40×10^{16} to 110×10^{16} mg^{-1} for zircons with ages between 440 and 480 Ma. These α-dose values correspond to FWHM in the 1008 cm^{-1} peak ranging up to 14 cm^{-1}, as observed here. Therefore, we conclude all the zircons measured in this study are metamict. However, we decided to explore the extent of inclusion pressure and the influence of radiation damage. We caution readers that the zircon-in-garnet results from this work cannot be used for quantitative temperature constraints.

Raman frequency shift was calculated for 201, 213, 224, 356, 438, 975, and 1008 cm^{-1} bands relative to unstrained zircon reference (NMNH 117288-3) (Supplementary File—Table S4). In most Sierra Valle Fértil-La Huerta samples the magnitude of the Raman shift varies significantly among inclusions from the same sample. Residual pressure (P_{inc}) calculated using each inclusion's frequency shifts produce a wide range of values from 520 to 149 MPa (Fig. 10). Zircon residual pressures (P_{inc}) was calculated by accounting for residual strain components at ambient temperature (Angel et al. 2019; Stangarone et al. 2019) and applying hydrostatic calibrations specific to 1008, 975, and 438 cm^{-1} bands (Zhong et al. 2019). All inclusions exhibit positive P_{inc} values, but some variability is observed when comparing the two methods. When employing the hydrostatic method (P_{inc}^{H}), there are significant dissimilarities between P_{inc} values calculated using the $\Delta\omega_{1008}$, $\Delta\omega_{975}$ and $\Delta\omega_{438}$ shifts. Generally, $\Delta\omega_{1008}$ and $\Delta\omega_{975}$ calculations aligned whereas the $\Delta\omega_{438}$ shifts exhibit further variability with differences exceeding 600 MPa. Moreover, the $\Delta\omega_{1008}$ and $\Delta\omega_{975}$ calculations are consistent with results from the strain components method (P_{inc}^{S}). Using those bands, we find no significant differences between these two calculation methods for most inclusions. Consequently, the calculated entrapment temperatures differ by <100 °C between hydrostatic and strain components methods. Zircon is characterized by its tetragonal structure, and similar to quartz, exhibits two symmetry-independent strains: $\varepsilon_1 = \varepsilon_2$ and ε_3 (Stangarone et al. 2019). All but 5 zircon inclusions exist under compressive stress, primarily characterized by negative $\varepsilon_1 + \varepsilon_2$ and ε_3 components. Following Gonzalez et al. (2019), 22 zircon inclusions present isotropic strain ($A = \pm 0.001$). There is no correlation between inclusion pressure variability, radiation damage, and elastic anisotropy strain. Calculated entrapment temperatures from the zircon inclusions exhibit extreme variability. Strain components and 1008 cm^{-1} band hydrostatic calibration yield values from 691 to 1574 °C and 746 to 1581 °C, respectively. These results consistently exceed the estimations from conventional thermobarometry by >100 °C, and some permissible ranges even exceed 1000 °C.
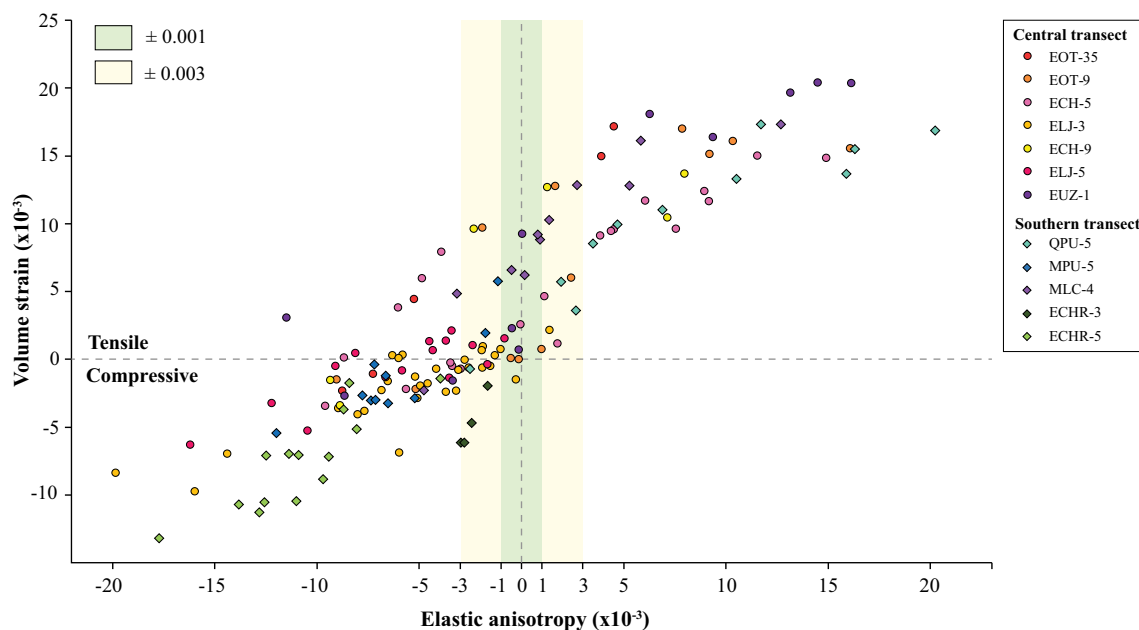
Fig. 8 Comparison between elastic anisotropy and volume strain. *Green* and *yellow* domains show the threshold of ±0.001 and ±0.003 for isotropic inclusions. Inclusions with positive volume strain are under tensile stress whereas inclusions with negative volume strain are under compressive stress (color figure online)

For example, EUZ-1 inclusions display a wide range of entrapment temperatures ranging from 623 to 1550 °C, in contrast to the 650 °C from previous studies.

Discussion

The Sierra Valle Fértil-La Huerta section provides an ideal testing ground to evaluate the effectiveness of elastic thermobarometry in comparison to conventional thermobarometric methods. Our large-scale comparison reveals differences between methods. Elastic thermobarometry commonly underestimates or overestimates entrapment pressures or temperatures established by conventional thermobarometry (Figs. 7, 8, and 12). The mismatch holds true even when using only our most suitable isotropic inclusions. Entrapment pressures tend to differ by >100 MPa on isotropic inclusions, which increases to >200 MPa for anisotropic inclusions. Entrapment temperatures also exhibit a similar behavior, with high variability and overestimation of temperatures compared to conventional results.

Although the precise comparison of elastic and conventional thermobarometry at specific sites is hampered by lack of data from the exact same hand samples, elastic thermobarometry does approximate the general expectations for P–T conditions when considering the full Sierra Valle Fértil-La Huerta section (Fig. 9). The highest pressures are found in rocks located in the western and central areas, the most mafic areas that represent the deepest parts

of the crustal section. The lowest pressures are observed in rocks in the eastern, upper crustal silicic unit. Moreover, our samples collected at similar paleo-depths along the separate central and southern transects produce similar entrapment pressures. For instance, the central ELJ-3 and the southern MPU-5 samples are both located within the transitional zone between the mafic and intermediate units, and Raman barometry indicates that both formed at similar pressures (1087 ± 41 and 1097 ± 67 MPa, respectively). Elastic thermobarometry best reproduces results from conventional thermobarometry in the two samples from the relatively low-temperature, high-pressure rocks from Sierra Loma de las Chacras (Fig. 9). Las Chacras block is a small forearc section of the Famatianian arc that was under-trusted beneath the plutonic column (>45 km) by collisional convergence, but tectonically extruded during orogenic collapse (Cristofolini et al. 2014; Mulcahy et al. 2014). Conventional thermobarometry results predict PT conditions of 650–850 °C and 900–1300 MPa (Mulcahy et al. 2014). Our Raman data suggest entrapment pressures from 780 to 1307 MPa.

Factors affecting residual pressure

Elastic thermobarometry does not well reproduce estimates from conventional thermobarometry in the Sierra Valle Fértil-La Huerta, but it provides similar results at Sierra Loma de Las Chacras. We believe that our results from Sierra Valle Fértil-La Huerta and Loma de Las Chacras provide an opportunity to assess geologic processes that may
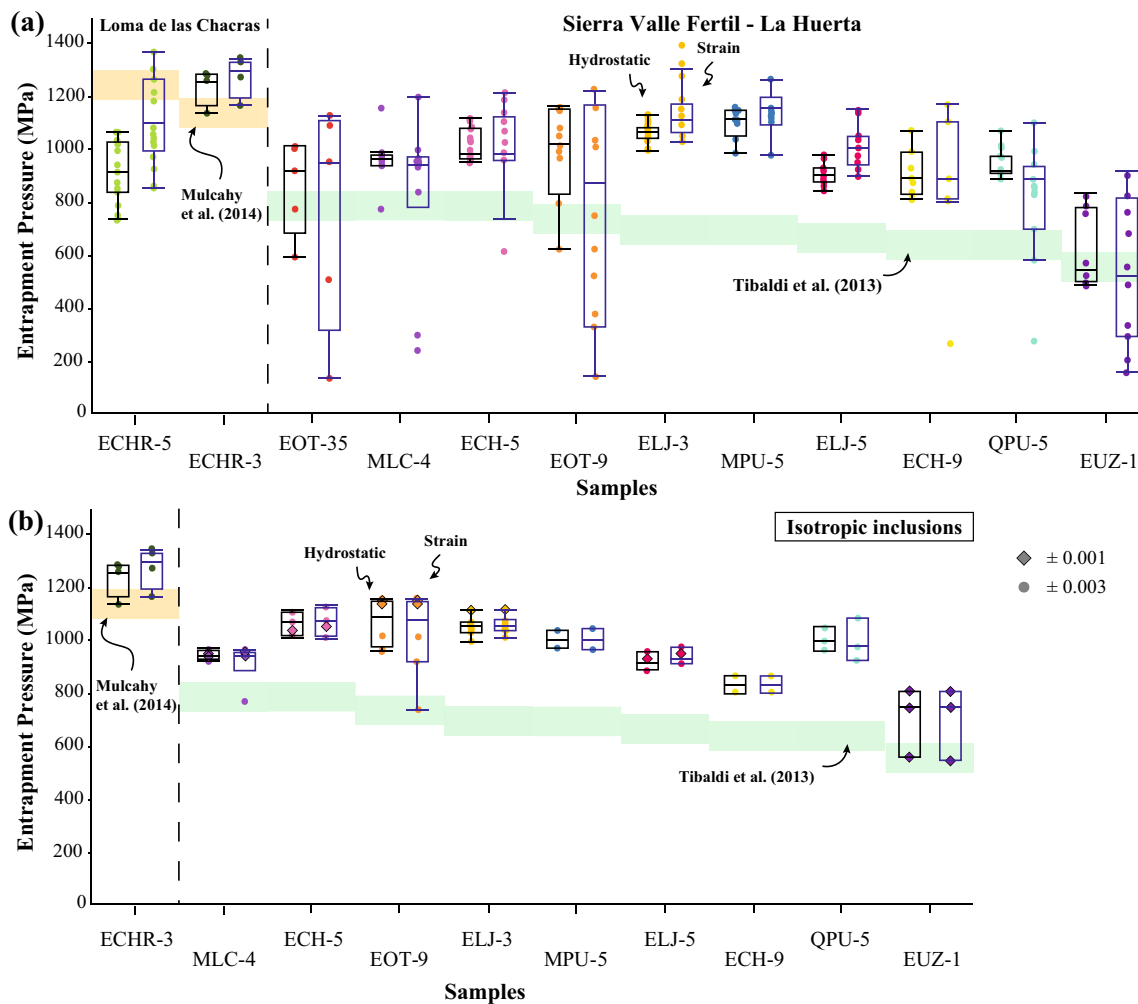
Fig. 9 **a** Whisker plot showing the distribution of calculated entrapment pressures for all the samples from Sierra Valle Fértil-La Huerta and Sierra Loma de las Chacras. **b** Whisker plot with entrapment pressure results from inclusions with isotropic strain produce tighter ranges and better matches. *Rhombus* represent inclusions with isotropic strain (± 0.001) and *circles* represent inclusion with some elastic strain anisotropy (± 0.003). *Green and yellow domains* highlight the PT estimations from previous conventional thermobarometry studies (Tibaldi et al. 2013; Mulcahy et al. 2014) (color figure online)

modify P–T estimates deduced from elastic thermobarometry. In the following discussion, we explore mechanisms that may have modified the elastic fidelity of the host-inclusion systems in the Sierra Valle Fértil-La Huerta and Sierra Loma de Las Chacras. We acknowledge that this list is not exhaustive, and was chosen to present the most likely alteration factors for quartz and zircon inclusions that operated specifically during the evolution of the Famatinian Arc.

Negative inclusion pressure and hydrostatic calibration

Empirical investigations exploring the formation and maintenance of negative inclusion pressures do not provide insight because they do not exist. Hydrostatic Raman calibrations were one of first methods employed to estimate the pressure preserved by inclusions in host minerals. Schmidt

and Ziemann (2000) studied the in-situ Raman frequency shift of quartz under hydrostatic pressure using a diamond-anvil cell. Based on experimental data, Schmidt and Ziemann (2000) developed calibrated equations that established the relationship between increasing pressure and frequency shift for the 128, 206, and 464 cm^{-1} bands. These hydrostatic calibrations covered a range of pressures between 0.1 and 2100 MPa at 23 °C. Increasing pressure creates a shift toward higher wavenumbers for each Raman band. Consequently, these hydrostatic calibration equations are only constrained for inclusions that are immersed under a compressive hydrostatic stress field, and present a positive frequency shift.

Negative frequency shift is observed in >80% of the inclusions analyzed in this study. We have no calibration for negative shifts because hydrostatic experiments
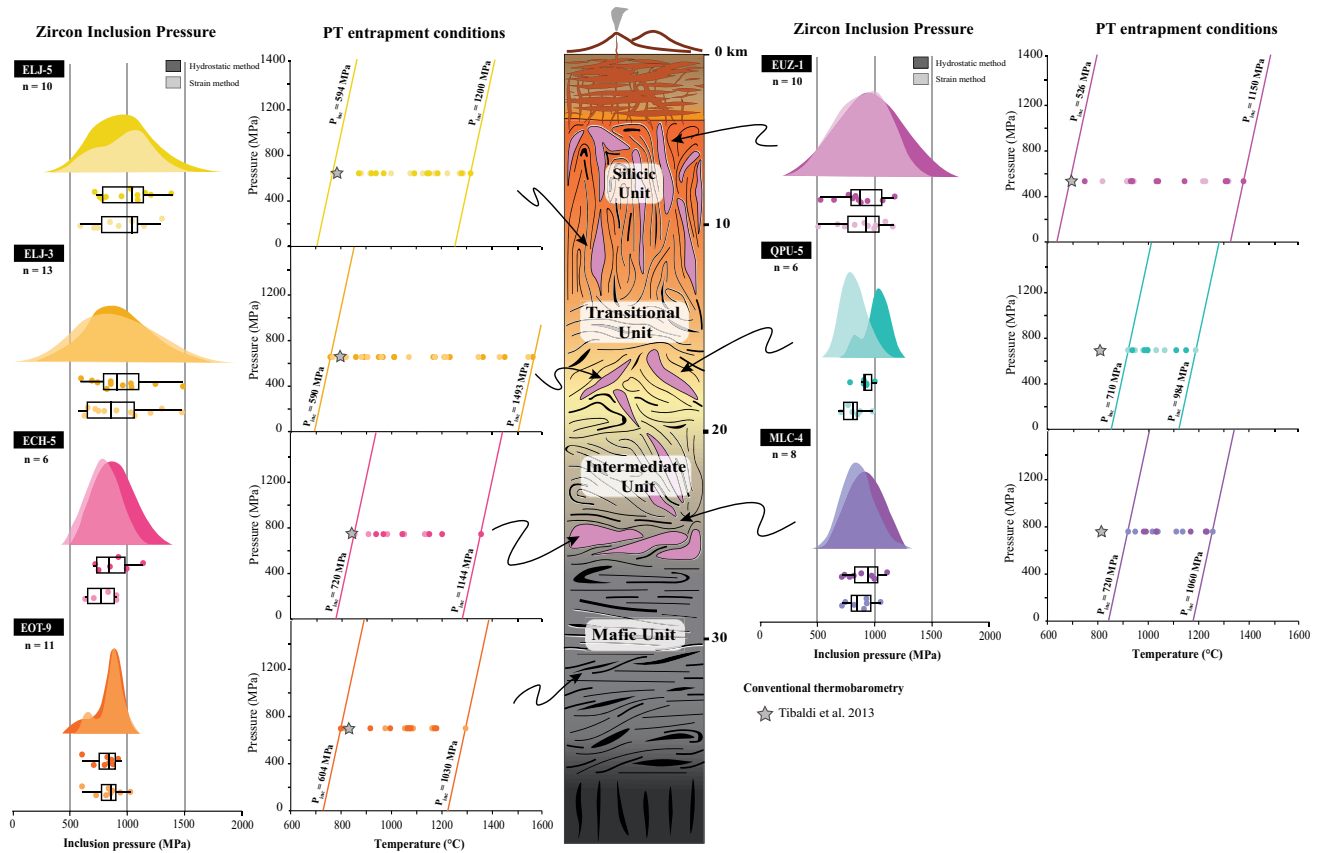
Fig. 10 Raincloud diagram of inclusion pressure distribution and calculated inclusion pressure isomekes of zircon inclusions. Relative location of each sample is indicated in a schematic reconstruction of the Famatinian Arc crustal section, showing the distribution of the different lithological units. Raincloud diagrams compare P_{inc} results from hydrostatic and strain components methods. Maximum and minimum P_{inc} are indicated with *colored* isomekes lines. The *colored points* indicate entrapment temperatures constrained with previous pressure estimates from conventional thermobarometry (*gray stars*) (color figure online)

on minerals under tensile condition have never been conducted. Following Kouketsu et al. (2014), we estimated inclusion pressure by extrapolating the hydrostatic calibration equation from Schmidt and Ziemann (2000) into the negative range, obtaining negative inclusion pressures. Kouketsu et al. (2014) found that the negative extrapolation successfully reproduces expected pressures for the majority of the experimental samples. Some negative frequency shifts in the 206 and 128 cm^{-1} bands did not match. However in our samples negative P_{inc} from the rare isotropic quartz inclusions always reproduces P_{inc} obtained using the strain tensor method, to within 25 MPa. This indicates that the extrapolated hydrostatic equations, even when applied to negative frequency shifts, likely recover entrapment pressures. Like Kouketsu et al. (2014), intrasample P_{inc} is less consistent using the 206 cm^{-1} band. Other bands tend to be consistent to within 100 MPa. Therefore, the hydrostatic method as applied to isotropic spherical inclusions inside an isotropic host offers a reasonable approximation for estimating inclusion pressure

despite calibrations not extending to negative pressures. Nonetheless, we recognize that until an equation is specifically calibrated for negative Raman shift, the result should be treated with caution and always compared to another method to verify their accuracy.

Quartz alpha–beta transition and tensile strain

The α–β phase transition may significantly limit quartz-in-garnet elastic thermobarometry at high temperatures. The α–β transition represents the change from low rhombohedral, α-quartz to high-temperature, hexagonal β-quartz. At 0.1 MPa this transition occurs at approximately 573 °C, and the slope of the transition increases linearly at a rate of 0.255 °C MPa^{-1} (Schmidt and Ziemann 2000; Johnson et al. 2021). This phase transition introduces large non-linear variations in mineral volume and density. When transitioning from α-quartz to β-quartz, there is ~0.63% volumetric expansion and linear anisotropic extensional strains of 0.24 and 0.14% along the principal a ($\varepsilon_1 + \varepsilon_2$) and c (ε_3) axis,

respectively (Carpenter et al. 1998; Johnson et al. 2021). These changes are expected to be reversible. Quantifying the P–T–V behavior of quartz during this phase transition is complicated because of the structural phase change and the development of spontaneous strains (Angel et al. 2017a; Gonzalez et al. 2024). Recent elastic models have incorporated these variations, but there are still significant uncertainties in entrapment calculations, primarily deriving from the unusual behavior of elastic properties such as compressibility and thermal expansivity (Cesare et al. 2021; Mazzucchelli et al. 2021).

Conventional thermobarometry at Sierra Valle Fértil-La Huerta suggests that peak metamorphic conditions in metapelites reached or exceeded the α–β quartz phase transition. Many samples likely reached the stability field of β-quartz. Samples with reference, conventional P–T conditions within the β-quartz field exhibit the highest variability and the most negative strains. These samples produce entrapment pressures with >200 MPa differences relative to conventional thermobarometry values (Supplementary File—Figs. S3, S4, and S5).

Previous studies on high-temperature quartz-in-garnet have attributed the large negative shift to drastic quartz volume reduction during the retrograde transition from β to α during cooling and exhumation (Nishiyama and Aikawa 2011; Kouketsu et al. 2014). The volume decrease induces tensile stress within the quartz inclusions, resulting in a pronounced negative $\Delta\omega$. The mechanisms underlying the formation of these stretched inclusions remain poorly understood. One potential explanation is the adhesion of the inclusion to the surrounding host, driven by nature's tendency to minimize surface energies (Ashley et al. 2015). However, the specific forces at play at the inclusion-host boundary and the bonding mechanism that securely attaches quartz to the adjacent garnet remain unknown. Nevertheless, it is evident that some form of bonding or adhesion must take place, as detachment of quartz from the garnet wall during exhumation would lead to the absence of a Raman frequency shift and the creation of a void space within the inclusion, observations that are not commonly reported in the literature.

Shape maturation on quartz inclusions

Diffusion-controlled shape maturation is a well-recognized phenomenon that occurs in fluid and melt inclusions at high temperatures (Gualda et al. 2012; Pamukcu et al. 2015). Previous studies have discovered that solid mineral inclusions can undergo similar modifications, creating shapes that reduce the overall interphase energy between the host and the inclusion (Toriumi 1979; Okamoto and Michibayashi 2005). These shape modifications have been observed on garnet-hosted quartz inclusions in metamorphic rocks at granulite facies ($T > 650$ °C) (Cesare et al. 2021). Shape

maturation acts to transform elongate irregular polycrystalline inclusions into increasingly polyhedral shapes, passing through stages of "necking down" as temperature increases (Cesare et al. 2021). In the Sierra Valle Fértil-La Huerta samples, quartz inclusions exhibit a wide range of morphologies, including highly irregular shapes, rounded ovoids, and perfect polyhedrons. We find that frequency shift variability correlates with the shape variations. Polyhedral inclusions present the most pronounced negative frequency shifts, and subsequently the most negative P_{inc} and high elastic anisotropies. Ovoid shapes present positive to low negative frequency shift values, with $P_{inc} \sim 0$ and near isotropic behavior (Fig. 11).

Shape maturation is expected to reset the elastic equilibrium of the mineral inclusion. Therefore, the residual pressure recorded through elastic barometry in a matured inclusion does not reflect the pressure at the time of entrapment, but rather the conditions when shape modification ceased in response to decreasing temperature (Zhong et al. 2020; Cesare et al. 2021). Following these criteria, we recalculated the entrapment pressure of the Sierra Valle Fértil-La Huerta and Sierra Loma de las Chacras samples at 650 °C instead of 700–800 °C, and found that the pressure estimates much better recover previous results established by conventional thermobarometry (Fig. 12). Improved correlation at lower temperatures suggests that elastic thermobarometry may rely upon a viscoelastic "closure temperature" analogous to those adopted in diffusion and geochronology studies.

Post-entrapment viscous and plastic modifications

Temperature also plays an important role enhancing viscous creep and plastic yield processes. Mechanical modification of the host phase would complicate elastic thermobarometry because the modifications may generate differential stresses or allow inclusions to relax (Zhang 1998; Zhong et al. 2020). Viscous creep depends on the P–T path of the rocks, garnet composition, and timescale (Zhong et al. 2020). In high grade metamorphic environments, viscous creep of the garnet hosts may partially reset the inclusion pressures on timescales of ~1 million years (Zhong et al. 2020). Moreover, partial or complete plastic relaxation of stresses around the inclusion can occur at temperatures above 650 °C, similarly on timescales of ~1 million years (Zhong et al. 2020; Campomenosi et al. 2021).

Such million-year timescales coincide with those of crystallization and mountain building, and thus could explain the variability in inclusion pressure in samples from Sierra Valle Fértil-La Huerta. Previous studies on Sierra Valle Fértil-La Huerta metapelites demonstrated that the rocks were subjected >700 °C for at least 4 million years (Otamendi et al. 2008; Tibaldi et al. 2011, 2013). Metapelites within the mafic unit experienced significantly
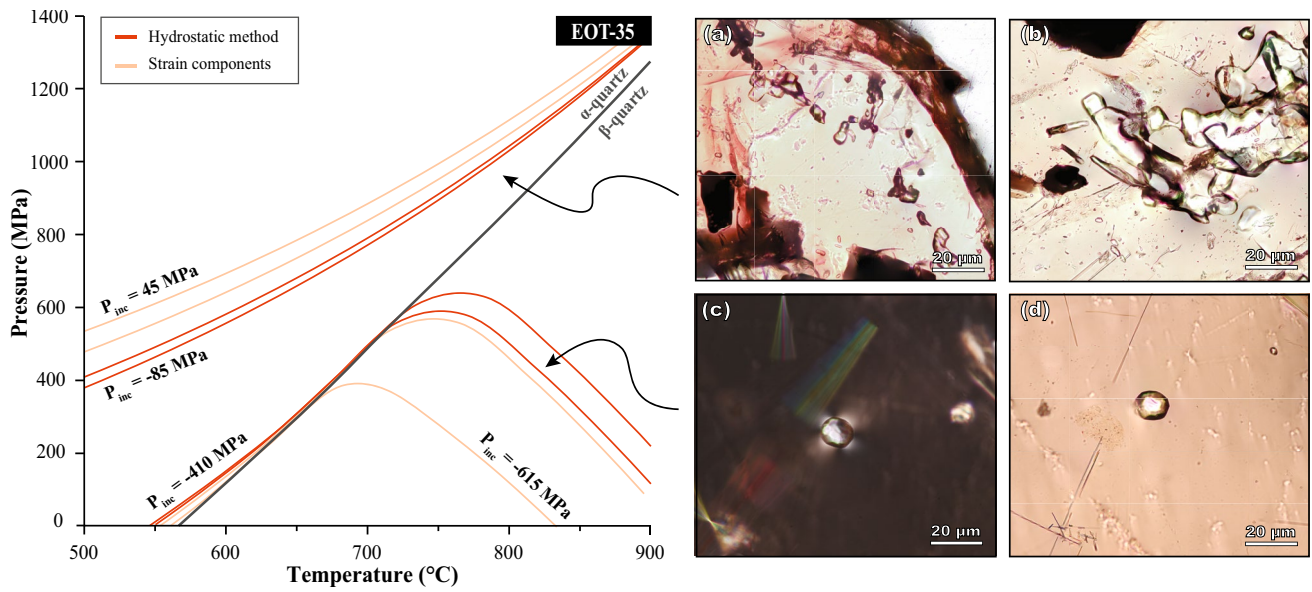
Fig. 11 Isomekes from EOT-35 sample with photomicrographs of the corresponding quartz inclusions. **a** and **b** Photomicrographs of polycrystalline irregular-shaped inclusions with "necking down" morphologies. **c** and **d** Photomicrographs of polyhedral quartz inclusions in cross (**c**) and plane polarized light (**d**) showing the characteristic stress-induced birefringence halo in the surrounding host. Quartz inclusions with positive P_{inc} exhibit irregular shapes (**a** and **b**) and inclusions with pronounced negative P_{inc} show polyhedral shapes (**c** and **d**)
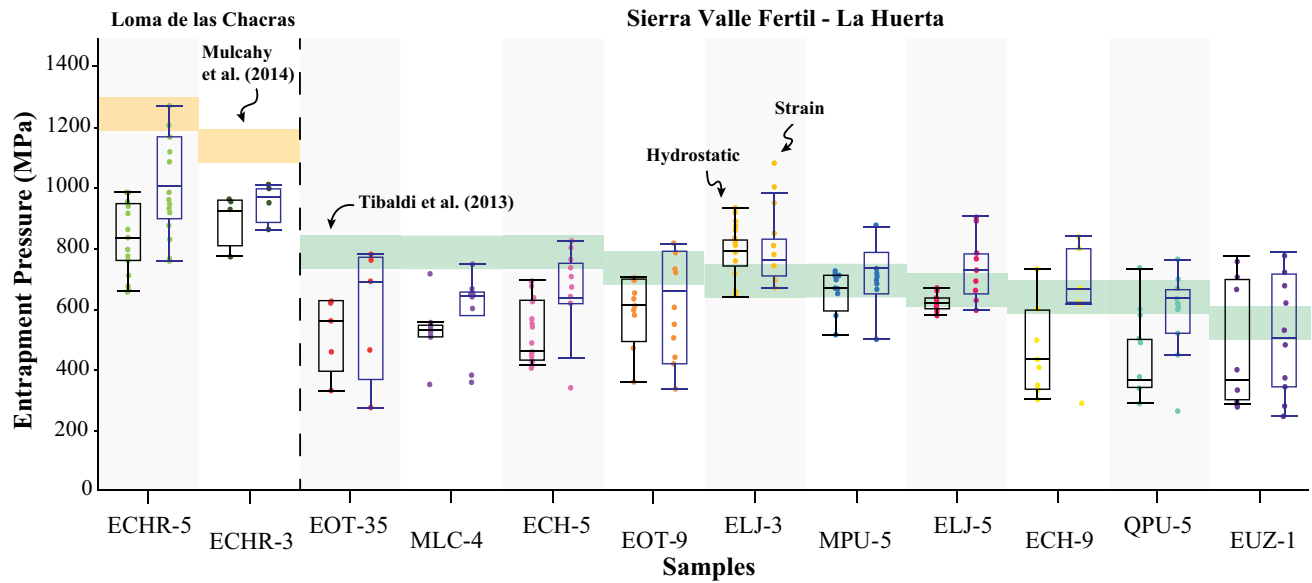
Fig. 12 Whisker plot showing the distribution of calculated entrapment pressures for all the samples from Sierra Valle Fértil-La Huerta and Sierra Loma de las Chacras at a closure temperature of 650 °C

higher temperatures than metapelites hosted within the silicic unit at shallower depths. Therefore, cross-arc temperature variations could explain the variability in the inclusion pressure, especially on samples from greater paleodepths and those nearer mafic igneous bodies. Viscous relaxation of garnet likely occurred in Sierra Valle Fértil-La Huerta. The viscous relaxation can explain both the variability of residual pressures and the tendency of the inclusions to have strain components near hydrostatic. Mechanisms can also work in concert. Viscous relaxation of host and shape maturation of inclusion could combine to reset the inclusions.

Fig. 13 Schematic P–T–t path of metasedimentary rock at Sierra Valle Fértil-La Huerta along with the evolution of quartz inclusions. t_0: Entrapment of quartz inclusions by garnet nucleation at growth. Quartz inclusions are polycrystalline irregular crystals. t_1: Metapelites reach metamorphic peak. Quartz inclusions underwent a volumetric expansion and shape maturation. t_2: Isobaric cooling of metapelites with quartz inclusions under a volumetric contraction
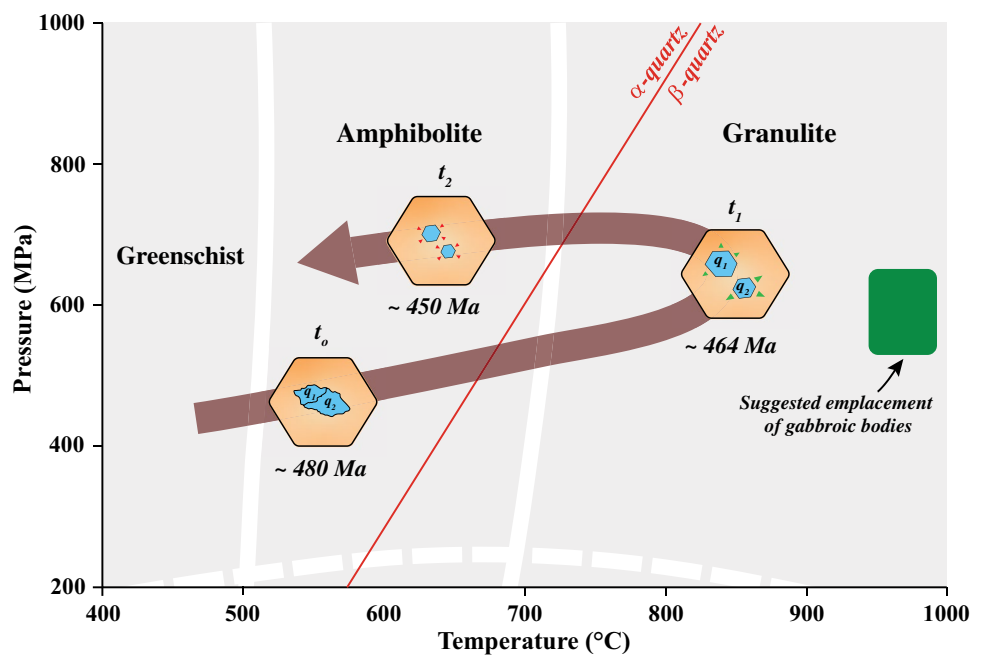
Geodynamic evolution of Sierra Valle Fértil-La Huerta

Using our new elastic thermobarometry results we summarize the P–T–t path of quartz and zircon inclusions in the context of the geodynamic evolution of Sierra Valle Fértil-La Huerta (Fig. 13). During the process of arc build-up from 491 to 474 Ma metasedimentary rocks from the pre-existing crust underwent a significant metamorphic prograde, reaching granulite facies approximately 2 Ma after the magmatic peak of the arc at ~474 Ma (Otamendi et al. 2008, 2020; Cristofolini et al. 2012; Ducea et al. 2017; Cornet et al. 2022). During this period, quartz and zircon inclusions were entrapped by garnet nucleation and growth, at temperatures ranging from 550 to 650 °C and pressures of 400 to 500 MPa. Zircon inclusions were entrapped isolated euhedral crystals whereas quartz inclusions were primarily entrapped as polycrystalline irregular grains. Quartz and zircon inclusions were subjected to a compressive stress field during that interval.

The intense magmatism led to an isobaric heating of metasedimentary rocks reaching the metamorphic peak conditions with temperatures between 800 and 870 °C and pressures between 500 and 800 MPa at ~464 Ma (Gallien et al. 2012; Ducea et al. 2017). During this isobaric interval quartz inclusions underwent shape maturation towards perfect polyhedral inclusions. Quartz underwent volume expansion in response to the transition from α to β quartz (e.g., Cesare et al. 2021). Moreover, partial resetting of residual strain in quartz and zircon inclusion might have occurred

because of viscous creep and plastic relaxation in the host garnet (Zhong et al. 2020).

With the beginning of the continental-to-arc collision the arc began to shut down (Cristofolini et al. 2014; Otamendi et al. 2020). Metasedimentary rocks followed an anticlockwise metamorphic P–T–t path that ended with a period of isobaric cooling, as inferred from mineral reaction textures and computed P–T pseudosections and diagrams (Otamendi et al. 2008; Gallien et al. 2012). The episode of cooling was slow and lasted ~10 Ma. During this phase the rocks crossed the α–β quartz phase transition again, causing quartz inclusions to contract. Contraction created a tensile stress field around the inclusions. The slow cooling rate may have contributed to the preservation of this tensile stress within the inclusions. Post-collisional deformation events from 437 to 409 Ma produced shear zones and tilted the entire arc, resulting in the exhumation and cooling of the entire crustal section (Cristofolini et al. 2014).

Declarations

Conflict of interest The authors declare that they have no conflict of interest.

References

Adams HG, Cohen LH, Rosenfeld JL (1975) Solid inclusion piezo-thermometry I: comparison dilatometry. Am Miner 60:574–583

Alvaro M, Mazzucchelli ML, Angel RJ, Murri M, Campomenosi N, Scambelli M, Nestola F, Korsakov A, Tomilenko AA, Marone F, Morana M (2020) Fossil subduction recorded by quartz from the coesite stability field. Geology 48:24–28. https://doi.org/10.1130/G46617.1

Angel RJ, Alvaro M, Nestola F, Mazzucchelli ML (2015a) Diamond thermoelastic properties and implications for determining the pressure of formation of diamond–inclusion systems. Russ Geol Geophys 56:211–220. https://doi.org/10.1016/J.RGG.2015.01.014

Angel RJ, Nimis P, Mazzucchelli ML, Alvaro M, Nestola F (2015b) How large are departures from lithostatic pressure? Constraints from host–inclusion elasticity. J Metamorph Geol 33:801–813. https://doi.org/10.1111/JMG.12138

Angel RJ, Mazzucchelli ML, Alvaro M, Nestola F (2017b) EosFit-Pinc: a simple GUI for host-inclusion elastic thermobarometry. Am Miner 102:1957–1960. https://doi.org/10.2138/am-2017-6190

Angel RJ, Murri M, Mihailova B, Alvaro M (2019) Stress, strain and Raman shifts. Z Kristallogr Cryst Mater 234:129–140. https://doi.org/10.1515/zkri-2018-2112

Angel RJ, Alvaro M, Miletich R, Nestola F (2017a) A simple and generalised P–T–V EoS for continuous phase transitions, implemented in EosFit and applied to quartz. Contrib Mineral Petrol 172. https://doi.org/10.1007/s00410-017-1349-x

Armas P, Cristofolini EA, Otamendi JE, Tibaldi AM, Barzola MG, Camilletti GC (2018) Geochronology and facies analysis of subaqueous volcanism of lower ordovician, Famatinian arc, Argentina. J South Am Earth Sci 84:255–265. https://doi.org/10.1016/J.JSAMES.2018.04.005

Armas P, Cristofolini E, Escribano F, Camilletti GC, Barzola M, Otamendi JE, Cisterna C, Leisen M, Romero R, Barra F, Tibaldi A (2021) Lower-middle ordovician sedimentary environment and provenance of the suri formation in the northern region of the Famatina belt, Catamarca. Argentina J South Am Earth Sci 105:102948. https://doi.org/10.1016/J.JSAMES.2020.102948

Ashley KT, Caddick MJ, Steele-Macinnis MJ, Bodnar MJ, Dragovic B (2014) Geothermobarometric history of subduction recorded by quartz inclusions in garnet. Geochem Geophys Geosyst 15:350–360. https://doi.org/10.1002/2013GC005106

Ashley KT, Darling RS, Bodnar RJ, Law RD (2015) Significance of "stretched" mineral inclusions for reconstructing P-T exhumation history. Contrib Miner Petrol 169:55. https://doi.org/10.1007/s00410-015-1149-0

Ashley KT, Steele-MacInnis M, Bodnar RJ, Darling RS (2016) Quartz-in-garnet inclusion barometry under fire: reducing uncertainty from model estimates. Geology 44:699–702. https://doi.org/10.1130/G38211.1

Astini RA, Dávila FM (2004) Ordovician back arc foreland and Ocloyic thrust belt development on the western Gondwana margin as a response to Precordillera terrane accretion. Tectonics 23. https://doi.org/10.1029/2003TC001620

Baldwin SL, Schönig J, Gonzalez JP, Davies H, Eynatten HV (2021) Garnet sand reveals rock recycling processes in the youngest exhumed high-and ultrahigh-pressure terrane on Earth. Proc Natl Acad Sci USA 118(3). https://doi.org/10.1073/pnas.2017231118

Barkoff DW, Ashley KT, Da Silva RG, Mazdab FK, Steele Macinnis M (2019) Thermobarometry of three skarns in the ludwig area, Nevada, based on raman spectroscopy and elastic modeling of mineral inclusions in garnet. Can Mineral 57:25–45. https://doi.org/10.3749/canmin.1800050

Bass JD (1995) Elasticity of minerals, glasses, and meltsin mineral physics & crystallography, TJ Ahrens (ed). https://doi.org/10.1029/RF002p0045

Binvignat FAP, Malcherek T, Angel RJ, Paulmann C, Schlüter J, Mihailova B (2018) Radiation-damaged zircon under high pressures. Phys Chem Miner 45:981–993. https://doi.org/10.1007/s00269-018-0978-6

Bonazzi M, Tumiati S, Thomas JB, Angel RJ, Alvaro M (2019) Assessment of the reliability of elastic geobarometry with quartz inclusions. Lithos 350–351:105201. https://doi.org/10.1016/J.LITHOS.2019.105201

Camilletti G, Otamendi J, Tibaldi A, Cristofolini E, Leisen M, Romero R, Barra F, Armas P, Barzola M (2020) Geology, petrology and geochronology of Sierra Valle Fértil-La Huerta batholith: implications for the construction of a middle-crust magmatic-arc section. J South Am Earth Sci 97. https://doi.org/10.1016/j.jsames.2019.102423

Camilletti GC, Otamendi JE, Escribano FA, Cristofolini EA (2023) Petrological and chemical evidence for polybaric differentiation across the preserved middle crustal plutonic column of the Famatinian arc, Argentina. Int J Earth Sci 112:2025–2047. https://doi.org/10.1007/S00531-023-02339-W/FIGURES/12

Campomenosi N, Mazzucchelli ML, Mihailova B, Scambelluri M, Angel RJ, Nestola F, Reali A, Alvaro M (2018) How geometry and anisotropy affect residual strain in host-inclusion systems: coupling experimental and numerical approaches. Am Miner 103:2032–2035. https://doi.org/10.2138/am-2018-6700CCBY

Campomenosi N, Rubatto D, Hermann J, Mihailova B, Scambelluri M, Alvaro M (2020) Establishing a protocol for the selection of zircon inclusions in garnet for Raman thermobarometry. Am Miner 105:992–1001. https://doi.org/10.2138/am-2020-7246

Campomenosi N, Scambelluri M, Angel RJ, Hermann J, Mazzucchelli ML, Mihailova B, Piccoli F, Alvaro M (2021) Using the elastic properties of zircon-garnet host-inclusion pairs for thermobarometry of the ultrahigh-pressure Dora-Maira whiteschists: problems and perspectives. Contrib Miner Petrol 176:1–17. https://doi.org/10.1007/S00410-021-01793-6/FIGURES/6

Campomenosi N, Angel RJ, Alvaro M, Mihailova B (2023) Resetting of zircon inclusions in garnet: Implications for elastic thermobarometry. Geology 51:23–27. https://doi.org/10.1130/G50431.1

Carlson WD (2002) Scales of disequilibrium and rates of equilibration during metamorphism. Am Miner 87:185–204. https://doi.org/10.2138/AM-2002-2-301

Carpenter MA, Salje EKH, Graeme-Barber A, Wruck B, Dove MT, Knight KS (1998) Calibration of excess thermodynamic properties and elastic constant variations associated with the alpha <-> beta phase transition in quartz. Am Miner 83:2–22. https://doi.org/10.2138/am-1998-1-201

Casquet C, Rapela CW, Pankhurst RJ, Baldo E, Galindo C, Fanning CM, Dahlquist J (2012) Fast sediment underplating and essentially coeval juvenile magmatism in the Ordovician margin of Gondwana, Western Sierras Pampeanas, Argentina. Gondwana Res 22:664–673. https://doi.org/10.1016/j.gr.2012.05.001

Castro AE, Spear FS (2017) Reaction overstepping and re-evaluation of peak P-T conditions of the blueschist unit Sifnos, Greece: implications for the Cyclades subduction zone. Int Geol Rev 59:548–562. https://doi.org/10.1080/00206814.2016.1200499

Cesare B, Parisatto M, Mancini L, Peruzzo L, Franceschi M, Tacchetto T, Reddy S, Spiess R, Nestola F, Marone F (2021) Mineral inclusions are not immutable: Evidence of post-entrapment thermally-induced shape change of quartz in garnet. Earth Planet Sci Lett 555. https://doi.org/10.1016/j.epsl.2020.116708

Cisneros M, Befus KS (2020) Applications and limitations of elastic thermobarometry: insights from elastic modeling of inclusion-host pairs and example case studies. Geochem Geophys Geosyst 21. https://doi.org/10.1029/2020GC009231

Cisneros M, Barnes JD, Behr WM, Kotowski AJ, Stockli DF, Soukis K (2021) Insights from elastic thermobarometry into exhumation of high-pressure metamorphic rocks from Syros, Greece. Solid Earth 12:1335–1355. https://doi.org/10.5194/se-12-1335-2021

Cisneros M, Behr WM, Platt JP, Anczkiewicz R (2022) Quartz-in-garnet barometry constraints on formation pressures of eclogites from the Franciscan Complex, California. Contrib Mineral Petrol 2022 177:1–23. https://doi.org/10.1007/S00410-021-01876-4

Cizina MF, Mikesell TD, Kohn MJ (2023) Optimizing Raman spectral collection for quartz and zircon crystals for elastic thermobarometry. Am Miner 108:915–927. https://doi.org/10.2138/AM-2022-8423

Cornet J, Laurent O, Wotzlaw JF, Antonelli MA, Otamendi J, Bergantz GW, Bachmann O (2022) Reworking subducted sediments in arc magmas and the isotopic diversity of the continental crust: the case of the Ordovician Famatinian crustal section, Argentina. Earth Planet Sci Lett 595. https://doi.org/10.1016/j.epsl.2022.117706

Cristofolini EA, Otamendi JE, Ducea MN, Pearson DM, Tibaldi AM, Baliani I (2012) Detrital zircon U-Pb ages of metasedimentary rocks from Sierra de Valle Fértil: entrapment of Middle and Late Cambrian marine successions in the deep roots of the Early Ordovician Famatinian arc. J South Am Earth Sci 37:77–94. https://doi.org/10.1016/J.JSAMES.2012.02.001

Cristofolini EA, Otamendi JE, Walker BA, Tibaldi AM, Armas P, Bergantz GW, Martino RD (2014) A Middle Paleozoic shear zone in the Sierra de Valle Fértil, Argentina: Records of a continent-arc collision in the Famatinian margin of Gondwana. J South Am Earth Sci 56:170–185. https://doi.org/10.1016/J.JSAMES.2014.09.010

Ducea MN, Bergantz GW, Crowley JL, Otamendi J (2017) Ultrafast magmatic buildup and diversification to produce continental crust during subduction. Geology 45:235–238. https://doi.org/10.1130/G38726.1

Dunn JR, Fisher DW (1954) Occurrence, properties, and paragenesis of anthraxolite in the Mohawk Valley [New York]. Am J Sci 252:489–501. https://doi.org/10.2475/AJS.252.8.489

Ehlers AM, Zaffiro G, Angel RJ, Boffa-Ballaran T, Carpenter MA, Alvaro M, Ross NL (2022) Thermoelastic properties of zircon: implications for geothermobarometry. Am Miner 107:74–81. https://doi.org/10.2138/am-2021-7731

Enami M (2012) Influence of garnet hosts on the Raman spectra of quartz inclusions. J Mineral Petrol Sci 107:173–180. https://doi.org/10.2465/jmps.111216

Enami M, Nishiyama T, Mouri T (2007) Laser Raman microspectrometry of metamorphic quartz: a simple method for comparison of metamorphic pressures. Am Miner 92:1303–1315. https://doi.org/10.2138/am.2007.2438

Escribano FA, Cornet J, Camilletti GC, Otamendi JE, Armas P, Cristofolini EA, Bachmann O (2022) Generation of crystal-poor rhyolites from a shallow plutonic reservoir in the Famatinian arc (Argentina). J Volcanol Geoth Res 431:107644. https://doi.org/10.1016/J.JVOLGEORES.2022.107644

Essene EJ (1989) The current status of thermobarometry in metamorphic rocks. Geol Soc Lond Special Publ 43:1–44. https://doi.org/10.1144/GSL.SP.1989.043.01.02

Ferry JM, Spear FS (1978) Experimental calibration of the partitioning of Fe and Mg between biotite and garnet. Contrib Miner Petrol 66:113–117. https://doi.org/10.1007/BF00372150

Ferry JM, Watson EB (2007) New thermodynamic models and revised calibrations for the Ti-in-zircon and Zr-in-rutile thermometers. Contrib Miner Petrol 154:429–437. https://doi.org/10.1007/s00410-007-0201-0

Gallien F, Mogessie A, Hauzenberger CA, Bjerg E, Delpino S, Castro de Machuca B (2012) On the origin of multi-layer coronas between olivine and plagioclase at the gabbro-granulite transition, Valle Fértil-La Huerta Ranges, San Juan Province, Argentina. J Metamorph Geol 30:281–302. https://doi.org/10.1111/j.1525-1314.2011.00967.x

Gonzalez JP, Thomas JB, Baldwin SL, Alvaro M (2019) Quartz-in-garnet and Ti-in-quartz thermobarometry: methodology and first application to a quartzofeldspathic gneiss from eastern Papua New Guinea. J Metamorph Geol 37:1193–1208. https://doi.org/10.1111/JMG.12508

Gonzalez JP, Mazzucchelli ML, Angel RJ, Alvaro M (2021) Elastic geobarometry for anisotropic inclusions in anisotropic host minerals: Quartz-in-Zircon. J Geophys Res Solid Earth 126. https://doi.org/10.1029/2021JB022080

Gonzalez JP, Thomas JB, Mazzucchelli ML, Angel RJ, Alvaro M (2024) First evaluation of stiff-in-soft host–inclusion systems: experimental synthesis of zircon inclusions in quartz crystals. Contrib Miner Petrol 179:13. https://doi.org/10.1007/s00410-023-02081-1

Gualda GAR, Pamukcu AS, Ghiorso MS, Anderson AT, Sutton SR (2012) Timescales of Quartz crystallization and the longevity of the bishop giant magma body. PLoS ONE 7:37492. https://doi.org/10.1371/journal.pone.0037492

Guo J, Zheng J, Cawood PA, Weinberg RF, Ping X, Li Y (2021) Archean trondhjemitic crust at depth in Yangtze Craton: Evidence from TTG xenolith in mafic dyke and apatite inclusion pressure in zircon. Precambrian Res 354:106055. https://doi.org/10.1016/j.precamres.2020.106055

Harvey KM, Penniston-Dorland SC, Kohn MJ, Piccoli PM (2021) Assessing P-T variability in mélange blocks from the Catalina Schist: is there differential movement at the subduction interface? J Metamorph Geol 39:271–295. https://doi.org/10.1111/jmg.12571

Holland TJB, Powell R (2011) An improved and extended internally consistent thermodynamic dataset for phases of petrological interest, involving a new equation of state for solids. J Metamorph Geol 29:333–383. https://doi.org/10.1111/j.1525-1314.2010.00923.x

Isaak DG, Anderson OL, Oda H (1992) High-temperature thermal expansion and elasticity of calcium-rich garnets. Phys Chem Miner 19:106–120. https://doi.org/10.1007/BF00198608/METRICS

Javoy M (1977) Stable isotopes and geothermometry. J Geol Soc London 133:609–636. https://doi.org/10.1144/gsjgs.133.6.0609

Johnson SE, Song WJ, Cook AC, Vel SS, Gerbi CC (2021) The quartz α↔β phase transition: Does it drive damage and reaction in continental crust? Earth Planet Sci Lett 553:116622. https://doi.org/10.1016/j.epsl.2020.116622

Kohn MJ (2014) "Thermoba-Raman-try": Calibration of spectroscopic barometers and thermometers for mineral inclusions. Earth Planet Sci Lett 388:187–196. https://doi.org/10.1016/j.epsl.2013.11.054

Kohn MJ, Mazzucchelli ML, Alvaro M (2023) Elastic thermobarometry. Annu Rev Earth Planet Sci 51:331–366. https://doi.org/10.1146/ANNUREV-EARTH-031621-112720

Korsakov AV, Kohn MJ, Perraki M (2020) Applications of Raman spectroscopy in metamorphic petrology and tectonics. Elements 16:105–110. https://doi.org/10.2138/GSELEMENTS.16.2.105

Kośmińska K, Gilotti JA, McClelland WC, Coble MA, Thomas JB (2022) P-T–t path of unusual Garnet–Kyanite–Staurolite—amphibole schists, Ellesmere Island, Canada—Quartz inclusion in garnet barometry and monazite petrochronology. J Petrol 63. https://doi.org/10.1093/petrology/egac068

Kouketsu Y, Nishiyama T, Ikeda T, Enami M (2014) Evaluation of residual pressure in an inclusion-host system using negative frequency shift of quartz Raman spectra. Am Miner 99:433–442. https://doi.org/10.2138/am.2014.4427

Kretz R (1959) Chemical study of garnet, biotite, and hornblende from gneisses of southwestern Quebec, with emphasis on distribution of elements in coexisting minerals. J Geol 67:371–402. https://doi.org/10.1086/626594

Lanari P, Engi M (2017) Local bulk composition effects on metamorphic mineral assemblages. Rev Mineral Geochem 83:55–102. https://doi.org/10.2138/RMG.2017.83.3

Li B, Liebermann RC (2014) Study of the Earth's interior using measurements of sound velocities in minerals by ultrasonic interferometry. Phys Earth Planet Inter 233:135–153. https://doi.org/10.1016/J.PEPI.2014.05.006

Mazzucchelli ML, Burnley P, Angel RJ, Morganti S, Domeneghetti MC, Nestola F, Alvaro M (2018) Elastic geothermobarometry: corrections for the geometry of the host-inclusion system. Geology 46:231–234. https://doi.org/10.1130/G39807.1

Mazzucchelli ML, Angel RJ, Alvaro M (2021) EntraPT: an online platform for elastic geothermobarometry. Am Miner 106:830–837. https://doi.org/10.2138/am-2021-7693CCBYNCND

Mazzucchelli ML, Reali A, Morganti S, Angel RJ, Alvaro M (2019) Elastic geobarometry for anisotropic inclusions in cubic hosts. Lithos 350–351. https://doi.org/10.1016/j.lithos.2019.105218

Milani S, Angel RJ, Scandolo L, Mazzucchelli ML, Ballatan TB, Klemme S, Domeneghetti MC, Miletich R, Scheidl KS, Derzsi M, Tokar K, Prencipe M, Alvaro M, Nestola F (2017) Thermoelastic behavior of grossular garnet at high pressures and temperatures. Am Miner 102:851–859. https://doi.org/10.2138/am-2017-5855

Moecher DP, Sharp ZD (1999) Comparison of conventional and garnet-aluminosilicate-quartz O isotope thermometry; insights for mineral equilibration in metamorphic rocks. Am Miner 84:1287–1303. https://doi.org/10.2138/am-1999-0906

Mulcahy SR, Roeske SM, Mcclelland WC, Ellis JR, Jourdan F, Renne PR, Vervoort JD, Vujovich GI (2014) Multiple migmatite events and cooling from granulite facies metamorphism within the Famatina arc margin of northwest Argentina. Tectonics 33:1–25. https://doi.org/10.1002/2013TC003398

Nasdala L, Wenzel M, Vavra G, Irmer G, Wenzel T, Kober B (2001) Metamictisation of natural zircon: accumulaton versus thermal annealing of radioactivity-induced damage. Contrib Miner Petrol 141:125–144. https://doi.org/10.1007/S004100000235/METRICS

Nasdala L, Smith DC, Kaindl R, Ziemann MA (2004) Raman spectroscopy: Analytical perspectives in mineralogical research. Spectr Methods Mineral:281–343. https://doi.org/10.1180/EMU-NOTES.6.7

Nestola F, Zaffiro G, Mazzucchelli ML, Nimis P, Andreozzi GB, Periotto B, Princivalle F, Lenaz D, Secco L, Pasqualetto L, Logvinova AM, Soboley NV, Lorenzetti A, Harris JW (2019) Diamond-inclusion system recording old deep lithosphere conditions at Udachnaya (Siberia). Sci Rep 9:12586. https://doi.org/10.1038/s41598-019-48778-x

Nishiyama T, Aikawa K (2011) Implication of the residual pressure recorded in quartz inclusions in garnet from high T metamorphic terranes. Japan Geoscience Union Meeting SMP046-05

O'Reilly C, Parnell J (1999) Fluid flow and thermal histories for Cambrian-Ordovician platform deposits, New York: evidence from fluid inclusion studies. Geol Soc Am Bull 111:1884–1896

Okamoto A, Michibayashi K (2005) Progressive shape evolution of a mineral inclusion under differential stress at high temperature: example of garnet inclusions within a granulite-facies quartzite from the Lützow-Holm Complex, East Antarctica. J Geophys Res Solid Earth 110:1–16. https://doi.org/10.1029/2004JB003526

Otamendi JE, Tibaldi AM, Vujovich GI, Viñao GA (2008) Metamorphic evolution of migmatites from the deep Famatinian arc crust exposed in Sierras Valle Fértil–La Huerta, San Juan, Argentina. J South Am Earth Sci 25:313–335. https://doi.org/10.1016/J.JSAMES.2007.09.001

Otamendi JE, Ducea MN, Tibaldi AM, Bergantz GW, de la Rosa JD, Vujovich GI (2009a) Generation of tonalitic and dioritic magmas by coupled partial melting of gabbroic and metasedimentary rocks within the deep crust of the Famatinian magmatic arc, Argentina. J Petrol 50:841–873. https://doi.org/10.1093/PETROLOGY/EGP022

Otamendi JE, Vujovich GI, de la Rosa JD, Tibaldi AM, Castro A, Martino RD, Pinotti LP (2009b) Geology and petrology of a deep crustal zone from the Famatinian paleo-arc, Sierras de Valle Fértil and La Huerta, San Juan, Argentina. J South Am Earth Sci 27:258–279. https://doi.org/10.1016/j.jsames.2008.11.007

Otamendi JE, Cristofolini E, Tibaldi AM, Quevedo FI, Baliani I (2010) Petrology of mafic and ultramafic layered rocks from the Jaboncillo Valley, Sierra de Valle Fértil, Argentina: Implications for the evolution of magmas in the lower crust of the Famatinian arc. J South Am Earth Sci 29:685–704. https://doi.org/10.1016/J.JSAMES.2009.11.001

Otamendi JE, Ducea MN, Bergantz GW (2012) Geological, petrological and geochemical evidence for progressive construction of an arc crustal section, Sierra de Valle Fértil, Famatinian Arc, Argentina. J Petrol 53:761–800. https://doi.org/10.1093/PETROLOGY/EGR079

Otamendi JE, Tiepolo M, Walker BA, Cristofolini EA, Tibaldi AM (2016) Trace elements in minerals from mafic and ultramafic cumulates of the central Sierra de Valle Fértil, Famatinian arc, Argentina. Lithos 240–243:355–370. https://doi.org/10.1016/J.LITHOS.2015.11.009

Otamendi JE, Cristofolini EA, Morosini A, Armas P, Tibaldi AM, Camilletti GC (2020) The geodynamic history of the Famatinian arc, Argentina: a record of exposed geology over the type section (latitudes 27°–33° south). J South Am Earth Sci 100. https://doi.org/10.1016/j.jsames.2020.102558

Pamukcu AS, Gualda GAR, Bégué F, Gravley DM (2015) Melt inclusion shapes: Timekeepers of short-lived giant magma bodies. Geology 43:947–950. https://doi.org/10.1130/G37021.1

Pattison DRM, Tinkham DK (2009) Interplay between equilibrium and kinetics in prograde metamorphism of pelites: an example from the Nelson aureole, British Columbia. J Metamorph Geol 27:249–279. https://doi.org/10.1111/j.1525-1314.2009.00816.x

Platt JP, Behr WM (2011) Grainsize evolution in ductile shear zones: implications for strain localization and the strength of the lithosphere. J Struct Geol 33:537–550. https://doi.org/10.1016/J.JSG.2011.01.018

Powell R (1985) Geothermometry and geobarometry: a discussion. J Geol Soc London 142:29–38. https://doi.org/10.1144/GSJGS.142.1.0029

Powell R, Holland T (1994) Optimal geothermometry and geobarometry. Am Miner 79:120–133

Powell R, Holland TJB (2008) On thermobarometry. J Metamorph Geol 26:155–179. https://doi.org/10.1111/J.1525-1314.2007.00756.X

Ramos VA (2018) The Famatinian orogen along the protomargin of Western Gondwana: evidence for a nearly continuous Ordovician magmatic arc between Venezuela and Argentina. 133–161. https://doi.org/10.1007/978-3-319-67774-3_6

Rapela CW, Pankhurst RJ, Casquet C, Dahlquist JA, Fanning MC, Baldo EG, Galindo C, Alasino PH, Ramacciotti CD, Verdecchia SO, Murra JA, Basei MAS (2018) A review of the Famatinian Ordovician magmatism in southern South America: evidence of lithosphere reworking and continental subduction in the early proto-Andean margin of Gondwana. Earth Sci Rev 187:259–285. https://doi.org/10.1016/J.EARSCIREV.2018.10.006

Rawlinson N, Pozgay S, Fishwick S (2010) Seismic tomography: a window into deep Earth. Phys Earth Planet Inter 178:101–135. https://doi.org/10.1016/J.PEPI.2009.10.002

Rosenfeld JL, Chase AB (1961) Pressure and temperature of crystallization from elastic effects around solid inclusions in minerals? Am J Sci 259:519–541. https://doi.org/10.2475/AJS.259.7.519

Schmidt C, Ziemann MA (2000) In-situ Raman spectroscopy of quartz: a pressure sensor for hydrothermal diamond-anvil cell experiments at elevated temperatures. Am Miner 85:1725–1734. https://doi.org/10.2138/am-2000-11-1216

Selverstone J, Spear FS (1985) Metamorphic P-T paths from pelitic schists and greenstones from the south-west Tauern Window, Eastern Alps. J Metamorph Geol 3:439–465. https://doi.org/10.1111/j.1525-1314.1985.tb00329.x

Spear FS, Wolfe OM (2019) Implications of overstepping of garnet nucleation for geothermometry, geobarometry and P-T path calculations. Chem Geol 530:119323. https://doi.org/10.1016/j.chemgeo.2019.119323

Spear FS, Wolfe OM (2020) Revaluation of "equilibrium" P-T paths from zoned garnet in light of quartz inclusion in garnet (QuiG) barometry. Lithos 372–373:105650. https://doi.org/10.1016/J.LITHOS.2020.105650

Spear FS, Selverstone J, Hickmott D, Crowley P, Hodges KV (1984) P-T paths from garnet zoning: a new technique for deciphering tectonic processes in crystalline terranes. Geology 12(2):87–90. https://doi.org/10.1130/0091-7613(1984)12%3C87:PPFGZA%3E2.0.CO;2

Spear FS, Kohn MJ, Florence FP, Menard T (1990) A model for garnet and plagioclase growth in pelitic schists: implications for thermobarometry and P-T path determinations. J Metamorph Geol 8:683–696. https://doi.org/10.1111/j.1525-1314.1990.tb00495.x

Spear FS, Ashley KT, Webb LE, Thomas JB (2012) Ti diffusion in quartz inclusions: implications for metamorphic time scales. Contrib Miner Petrol. https://doi.org/10.1007/s00410-012-0783-z

Spear FS, Thomas JB, Hallett BW (2014) Overstepping the garnet isograd: a comparison of QuiG barometry and thermodynamic modeling. Contrib Miner Petrol 168:1–15. https://doi.org/10.1007/S00410-014-1059-6

Stangarone C, Angel RJ, Prencipe M, Campomenosi N, Mihailova B, Alvaro M (2019) Measurement of strains in zircon inclusions by Raman spectroscopy. Eur J Mineral 31:685–694. https://doi.org/10.1127/ejm/2019/0031-2851

Thomas WA, Astini RA (1996) The Argentine precordillera: a traveler from the Ouachita embayment of North American Laurentia. Science 273:752–757. https://doi.org/10.1126/science.273.5276.752

Thomas JB, Spear FS (2018) Experimental study of quartz inclusions in garnet at pressures up to 3.0 GPa: evaluating validity of the quartz-in-garnet inclusion elastic thermobarometer. Contrib Mineral Petrol 173. https://doi.org/10.1007/S00410-018-1469-Y

Thomas JB, Watson EB, Spear FS, Shemella PT, Nayak SK, Lanzirotti A (2010) TitaniQ under pressure: The effect of pressure and temperature on the solubility of Ti in quartz. Contrib Miner Petrol 160:743–759. https://doi.org/10.1007/S00410-010-0505-3

Tibaldi AM, Álvarez-Valero AM, Otamendi JE, Cristofolini EA (2011) Formation of paired pelitic and gabbroic migmatites: an empirical investigation of the consistency of geothermometers, geobarometers, and pseudosections. Lithos 122:57–75. https://doi.org/10.1016/J.LITHOS.2010.11.016

Tibaldi AM, Otamendi JE, Cristofolini EA, Baliani I, Walker BA, Bergantz GW (2013) Reconstruction of the early ordovician famatinian arc through thermobarometry in lower and middle crustal exposures, sierra de valle fértil, argentina. Tectonophysics 589:151–166. https://doi.org/10.1016/J.TECTO.2012.12.032

Tomkins HS, Powell R, Ellis DJ (2007) The pressure dependence of the zirconium-in-rutile thermometer. J Metamorph Geol 25:703–713. https://doi.org/10.1111/j.1525-1314.2007.00724.x

Toriumi M (1979) A mechanism of shape-transformation of quartz inclusions in albite of regional metamorphic rocks. Lithos 12:325–333. https://doi.org/10.1016/0024-4937(79)90024-0

Valley JW (2001) Stable isotope thermometry at high temperatures. Rev Mineral Geochem 43:365–413. https://doi.org/10.2138/GSRMG.43.1.365

van Staal CR, Vujovich GI, Currie KL, Naipauer M (2011) An Alpine-style Ordovician collision complex in the Sierra de Pie de Palo, Argentina: record of subduction of Cuyania beneath the Famatina arc. J Struct Geol 33:343–361. https://doi.org/10.1016/J.JSG.2010.10.011

Walker BA, Bergantz GW, Otamendi JE, Ducea MN, Cristofolini EA (2015) A MASH zone revealed: the mafic complex of the Sierra Valle Fértil. J Petrol 56:1863–1896. https://doi.org/10.1093/petrology/egv057

Wang Z, Ji S (2001) Elasticity of six polycrystalline silicate garnets at pressure up to 3.0 GPa. Am Miner 86:1209–1218. https://doi.org/10.2138/am-2001-1009

Whitney DL, Evans BW (2010) Abbreviations for names of rock-forming minerals. Am Miner 95:185–187. https://doi.org/10.2138/am.2010.3371

Wolfe OM, Spear FS (2018) Determining the amount of overstepping required to nucleate garnet during Barrovian regional metamorphism, Connecticut Valley Synclinorium. J Metamorph Geol 36:79–94. https://doi.org/10.1111/jmg.12284

Wolfe OM, Spear FS (2020) Regional quartz inclusion barometry and comparison with conventional thermobarometry and intersecting isopleths from the Connecticut Valley Trough, Vermont and Massachusetts, USA. J Petrol 61. https://doi.org/10.1093/petrology/egaa076

Wolfe OM, Spear FS, Harrison TM (2021) Pronounced and rapid exhumation of the Connecticut Valley Trough revealed through quartz in garnet Raman barometry and diffusion modelling of garnet dissolution–reprecipitation reactions. J Metamorph Geol 39:1045–1069. https://doi.org/10.1111/jmg.12601

Wolfe OM, Spear FS, Thomas JB, Hasegawa EM, Libby GT, Cheney JT (2023) Pressure–temperature evolution of the basement and cover sequences on Ios, Greece: evidence for subduction of the

Hercynian basement. J Metamorph Geol 41:1119–1141. https://doi.org/10.1111/jmg.12738

Yuan X, Mayanovic RA (2017) An empirical study on Raman peak fitting and its application to Raman quantitative research. Appl Spectrosc 71:2325–2338. https://doi.org/10.1177/0003702817721527

Zack T, Moraes R, Kronz A (2004) Temperature dependence of Zr in rutile: empirical calibration of a rutile thermometer. Contrib Miner Petrol 148:471–488. https://doi.org/10.1007/s00410-004-0617-8

Zhang Y (1998) Mechanical and phase equilibria in inclusion–host systems. Earth Planet Sci Lett 157:209–222. https://doi.org/10.1016/S0012-821X(98)00036-3

Zhang M, Salje EKH, Farnan I, Graeme-Barber A, Daniel P, Ewing RC, Clark AM, Leroux H (2000) Metamictization of zircon: Raman spectroscopic study. J Phys: Condens Matter 12:1915. https://doi.org/10.1088/0953-8984/12/8/333

Zhong X, Andersen NH, Dabrowski M, Jamtveit B (2019) Zircon and quartz inclusions in garnet used for complementary Raman thermobarometry: application to the Holsnøy eclogite, Bergen Arcs, Western Norway. Contrib Mineral Petrol 174. https://doi.org/10.1007/s00410-019-1584-4

Zhong X, Moulas E, Tajčmanová L (2020) Post-entrapment modification of residual inclusion pressure and its implications for Raman elastic thermobarometry. Solid Earth 11:223–240. https://doi.org/10.5194/se-11-223-2020